UNIVERSIDADE FEDERAL DE SANTA CATARINA
CENTRO TECNOLÓGICO DE JOINVILLE
GRADUATE PROGRAM IN MECHANICAL ENGINEERING AND SCIENCES

Letícia Cristófoli Duarte Silva

Development and Validation of Synthetic Rain for Testing of Automated Driving Systems on Outdoor Proving Ground

Joinville
2023

Letícia Cristófoli Duarte Silva

Development and Validation of Synthetic Rain for Testing of Automated Driving Systems on Outdoor Proving Ground

Dissertation of Graduate Program in Mechanical Engineering and Sciences of Centro Tecnológico de Joinville of Universidade Federal de Santa Catarina to obtain the title of Master in Engineering and Mechanical Sciences.
Advisor: Prof. Thiago Antonio Fiorentin, Dr.
Co-advisor: Prof. André Luís Condino Fujarra, Dr.

Joinville
2023

Ficha de identificação da obra elaborada pelo autor,
através do Programa de Geração Automática da Biblioteca Universitária da UFSC.

Silva, Leticia Cristofoli Duarte
Development and validation of synthetic rain for testing of automated driving systems on outdoor proving ground / Leticia Cristofoli Duarte Silva ; orientador, Thiago Antonio Fiorentin, coorientador, André Luís Condino Fujarra, 2023.
86 p.

Dissertação (mestrado) - Universidade Federal de Santa Catarina, Campus Joinville, Programa de Pós-Graduação em Engenharia e Ciências Mecânicas, Joinville, 2023.

Inclui referências.

1. Engenharia e Ciências Mecânicas. 2. Veículos automatizados. 3. Chuva artificial. 4. Sensores de percepção. I. Fiorentin, Thiago Antonio. II. Fujarra, André Luís Condino . III. Universidade Federal de Santa Catarina. Programa de Pós-Graduação em Engenharia e Ciências Mecânicas. IV. Título.

Letícia Cristófoli Duarte Silva

Development and Validation of Synthetic Rain for Testing of Automated Driving Systems on Outdoor Proving Ground

The present Master level work was evaluated and approved by the jury composed by the following members:

Prof. Andrea Carboni Piga, Dr.
Universidade Federal de Santa Catarina

Profa. Anelize Zomkowski Salvi, Dr.
Universidade Federal de Santa Catarina

Prof. Pablo Andretta Jaskowiak, Dr.
Universidade Federal de Santa Catarina

Prof. Roberto Silva Netto, Dr.
Faculdade de Engenharia de Sorocaba

We certified that this is the original and final version of the concluding work, which was judged appropriate to obtain the title of master of engineering and mechanical sciences.

Documento assinado digitalmente
Wagner Mauricio Pachekoski
Data: 20/12/2023 10:01:13-0300
CPF: ***.494.569-**
Verifique as assinaturas em https://v.ufsc.br

Prof. Wagner Maurício Pachekoski, Dr.
Coordenador of the course

Documento assinado digitalmente
Thiago Antonio Fiorentin
Data: 19/12/2023 14:20:18-0300
CPF: ***.053.219-**
Verifique as assinaturas em https://v.ufsc.br

Prof. Thiago Antonio Fiorentin, Dr.
Advisor

Joinville, December 14th, 2023.

ACKNOWLEDGEMENTS

I express my gratitude to the universe for granting me the privilege of being present in this moment. I am thankful for all the opportunities you have given me.

To God, my sincere gratitude for listening to my prayers, bringing peace to my heart, and empowering me to persist through the challenges.

I am deeply grateful to my family who has always supported me in all my decisions. The Leticia from Boqueirão, Curitiba, could never imagined that she would go so far. This dissertation stands as a symbol of personal growth and reconciliation with my past choices.

Professor Thiago Fiorentin, your guidance as my advisor and your willingness to embark on this journey with me, investing your trust before witnessing my work, are truly appreciated.

Professor Werner Huber, the opportunity to work at CARISSMA as a Student Assistant marked a significant turning point in my life, for which I am immensely grateful.

Maikol Drechsler and Yuri Poledna, your company during this journey have been invaluable. Maikol, your warm welcome to the topic of this dissertation and your assistance in collecting the experimental data, coupled with your availability to always answer my questions, were extremely important. Yuri, thank you for generously sharing your knowledge and coding processes with me, your endless support and attention to detail have been indispensable (no witches in this work). Without both of you, completing this dissertation would have been an arduous task. I am grateful for the shared coffees, stories, and laughter in the laboratory that brightened this journey.

Amanda Coradt, Andressa Moura and Julia Schenkel, thank you for being my confidants throughout this process.

I would like to acknowledge AWARE, DAAD, FAPESC, and RoadView for their financial support, which played a crucial role in the development of this dissertation, especially during my time in Germany.

Finally, I thank myself for never giving up and for trying to do my best in all the things that I committed myself to. Moving to another country and completing this dissertation within fifteen months of my Master's degree was a challenging achievement, - one-personal fulfillment.

Thank you.

"As you start to walk on the way,
the way appears."
(Rumi, 13th century)

RESUMO

Esta dissertação insere-se no domínio do desenvolvimento de sistemas de percepção para aplicações de condução automatizada, uma investigação fundamental para garantir a segurança e a eficiência de veículos autônomos. Os sistemas de percepção dependem da precisão dos sensores e dos algoritmos de tratamento de dados, o que requer testes rigorosos, especialmente em condições climáticas adversas como chuva, nevoeiro e neve. Assim, o principal objetivo desta dissertação é desenvolver e validar uma instalação de chuva sintética externa para facilitar o teste de sistemas automatizados em condições climáticas adversas. A metodologia propõe a geração de três intensidades diferentes de chuva artificial, que são validadas por comparação com dados reais de chuva, um modelo teórico e dados de chuva sintética gerados em ambiente interno. Este processo de validação envolve vários parâmetros, incluindo dados de um disdrômetro e de uma estação meteorológica. A chuva sintética demonstrou uniformidade satisfatória na área de teste, reproduzindo com sucesso as três intensidades de chuva propostas. Além disso, foi observado que o vento pode influenciar o processo de geração da chuva externa. Ao ser comparada com dados de chuva real e com um modelo teórico, os resultados obtidos mostraram-se com padrões similares. Em seguida, a chuva sintética externa apresentou maior similaridade com a chuva real do que a chuva sintética interna, evidenciando-se como um método de teste viável, controlado e reprodutível. Além disso, esse sistema viabiliza a coleta confiável de dados em condições climáticas adversas. Assim, foi realizado um estudo de caso com uma câmera, utilizando técnicas de inteligência artificial para detecção de objetos, com a finalidade de comparar o desempenho do algoritmo em condições de tempo com chuva e sem chuva. Observou-se que os resultados da detecção de objetos sob chuva sintética são inferiores, em que, o algoritmo classifica erroneamente os objetos. No caso estudado, ele detecta barco no lugar de carro. Análises adicionais revelam que a iluminação nas imagens é um fator significativo que influencia os resultados, o que destaca a importância desse aspecto para testes futuros. Os resultados deste trabalho contribuem para a compreensão dos efeitos da chuva na capacidade do algoritmo de percepção, representando um passo fundamental para assegurar a segurança dos veículos autônomos em condições meteorológicas adversas.

Palavras-chave: Chuva Artificial. Teste & Validação. Sensores de Percepção. Veículos Automatizados.

RESUMO EXPANDIDO

INTRODUÇÃO

Visão Zero, estratégia da Comissão Europeia para eliminar mortes ocasionadas no trânsito até 2050 (European Commission, 2019), tem sido um catalisador para o avanço no desenvolvimento de veículos autônomos. Esta revolução tecnológica visa melhorar a segurança rodoviária, reduzir o congestionamento, aumentar a acessibilidade e economizar energia (Brown et al., 2014), (Folsom, 2012), (Morrow et al., 2014). Com o avanço dos veículos automatizados a responsabilidade pela segurança está cada vez mais concentrada nos algoritmos incorporados nesses sistemas, consequentemente há o aumento da demanda por sensores de percepção robustos (Cui et al., 2022). Câmeras, radar e lidar são os principais sensores e desempenham papel crucial na percepção do ambiente para os sistemas de condução automatizada. A chuva foi identificada como um fator significativo em acidentes rodoviários, contribuindo para um aumento alarmante de até 70% em incidentes durante condições adversas (Cui et al., 2022). Sezgin et al. (2023) afirma que há a perda de desempenho dos sensores em condições de chuva, destacando a importância de avaliar a confiabilidade desses sensores em vários cenários. Testes rigorosos e a validação dos sensores de percepção se tornam essenciais, em que testes de campo são importantes, mas limitados por condições meteorológicas imprevisíveis. Nesse contexto, esta dissertação apresenta uma metodologia para gerar chuva sintética em instalações externas, oferecendo acessibilidade e custo-benefício quando comparados a sistemas de geração interna de chuva artificial. A contribuição deste trabalho viabiliza testes de campo externos em condições de tempo adversas, garantindo segurança, repetibilidade e eficiência. E ainda, os resultados contribuem para a compreensão dos efeitos da chuva na percepção dos sensores que compõem veículos automatizados.

OBJETIVOS

O objetivo geral desta dissertação é desenvolver e validar uma instalação externa de chuva sintética para testes de campo em veículos automatizados. Os objetivos específicos são: estabelecer um sistema móvel para gerar chuva sintetica em instalações externas; determinar a disposição do sistema para diferentes intensidades de chuva; validar essas intensidades para alcançar uma distribuição realista de gotas; e analisar a influência das condições de chuva na percepção dos sistemas de veículos autônomos.

METODOLOGIA

O CARISSMA Institute of Automated Driving, localizado em Ingolstadt, Alemanha, é onde os testes de geração da chuva sintética aconteceram através de aspersores de jardim. Os métodos de medição utilizados compreendem um disdrômetro, uma estação meteorológica e o método do metro quadrado, essenciais para compreender as características da chuva. Um teste preliminar é conduzido para avaliar o desempenho dos aspersores e estimar a capacidade da geração de chuva artificial no CARISSMA. Diferentes arranjos dos aspersores são analisados com o intuito de atingir intensidades variadas de chuva - baixa, média e alta. A avaliação abrange a medição da chuva por meio dos métodos mencionados, além da análise da uniformidade, sua sensibilidade ao vento e a confiabilidade dos sistemas de medição. Para validação, a chuva gerada neste trabalho é comparada com três contextos: modelo teórico, chuva sintética interna

e condições reais de chuva. Os dados de chuva sintética interna provém do CEREMA Pavin, uma instalação na França, e a referência teórica utilizada é o modelo de Marshall-Palmer (Marshall; Palmer, 1948). Para a entre a chuva sintética e a chuva real, o disdrometer coleta dados reais durante cinco dias e é utilizado o método RMSE para comparar as distribuições de gotas. A segunda parte do trabalho consiste na utilização da chuva sintética gerada para analisar os sensores de percepção empregados em veículos automatizados. Esta análise abrange um conjunto integrado de sensores, composto por duas câmeras, um radar e dois lidars. A coleta de dados é realizada em tempo seco e nas três intensidades de chuva geradas nesta dissertação, com medições efetuadas durante o dia e à noite. O procedimento de coleta de dados envolve a utilização de três alvos distintos: um modelo adulto masculino, um modelo de ciclista e um modelo de automóvel. Alvos para entender a reflexão dos sensores também são incorporados na coleta de dados. A posição dos alvos é caracterizada por duas variáveis principais. Primeiramente, a distância entre o alvo e a posição do sensor varia em relação ao eixo x da instalação do CARISSMA. A segunda variável refere-se à orientação dos alvos, definida em ângulos de $0°$, $45°$ e $90°$ em relação à origem do alvo. Cada teste possui um período de aquisição de dados de 30 segundos, totalizando 176 testes. A análise de dados concentra-se na câmera RGB, visto que, apresenta notável sensibilidade à chuva em comparação com os demais sensores. Além disso, a maturidade dos algoritmos de tratamento de dados para câmeras é mais avançada do que os algoritmos de percepção utilizados em radar e lidar. O estudo foca especificamente no pacote de dados do modelo do carro, escolhido por representar a interação mais próxima com os sensores em cenários do mundo real. O objetivo central é identificar discrepâncias na detecção de objetos com base em diferentes parâmetros de posição do alvo e avaliar o impacto da chuva. Assim, dentre os testes realizados, aqueles conduzidos durante o dia e com uma orientação de $0°$ foram selecionados para esta análise comparativa, considerando que são mais representativos das interações automotivas usuais. Para realizar a análise, são considerados onze casos. Em cada episódio, é feita a abertura da imagem da câmera para identificação das coordenadas da caixa delimitadora do carro (esquerda, inferior, direita, superior), realizada manualmente. Posteriormente, o YOLO V7 é executado para determinar as informações da classe e extrair as caixas delimitadoras dos objetos. A avaliação é conduzida utilizando a técnica de mAP (Cartucho et al., 2018), que busca medir a concordância entre a caixa real do objeto e as caixas detectadas. Valores mais elevados de mAP indicam uma maior precisão na detecção de objetos entre classes. A comparação dos resultados de cada teste, permite a discussão sobre a influência da chuva e da distância do alvo na detecção de objetos.

RESULTADOS E DISCUSSÃO

Com o volume de água medido nas cinco posições da análise preliminar dos aspersores, as intensidades de chuva podem ser visualizadas. O aspersor rotativo demonstra uma distribuição uniforme das gotas de água ao longo de todo seu raio efetivo, assim é o equipamento selecionado para a geração de chuva. Para facilitar o cálculo sequencial do arranjo dos aspersores rotativos, a intensidade de chuva de um aspersor é assumida como $5\,\mathrm{mm/h}$, uma média aproximada das cinco posições. Além disso, as intensidades de chuva apresentadas são mais elevadas nas posições iniciais, então, é essencial um planejamento cuidadoso da disposição dos aspersores para garantir que estes se complementam entre si e proporcionam uma distribuição uniforme da água pela instalação de ensaio. A conclusão é que os aspersores devem ser colocados em pares, compensando a tendência decrescente do volume de água com o aumento do raio efetivo do equipamento. As análises da chuva sintética mostram que a maioria das gotas nas três intensidades se concentram no intervalo de diâmetro de $1\,\mathrm{mm}$ a $2\,\mathrm{mm}$. Em comparação, a

ocorrência de gotas maiores é menos frequente, e não há gotas maiores do que 4mm. Nota-se que o número total de gotas permanece relativamente elevado para diâmetros inferiores a 2 mm, e os picos são maiores à medida que a intensidade aumenta. Portanto, os resultados exibem um padrão coerente, destacando a curva de 25 mm/h, que converge entre as outras duas intensidade de chuva. Os aspersores foram capazes de fornecer água durante toda a aquisição de dados e as intensidades de chuva de 10 mm/h e 25 mm/h apresentaram melhores resultados de uniformidade sobre a área do segmento. Os mapas de calor para as três intensidades mostram uma influência significativa de fatores externos nas medições da chuva e os valores desiguais não se limitam apenas à quantificação esperada que difere pela posição dos aspersores, mas também revelam a influência do vento durante os testes, o que justifica as regiões mais claras dos mapas de calor. Os dados do vento para as três intensidades de chuva da estação meteorológica são apresentados, juntamente com a média das medições da intensidade da chuva utilizando o método do metro quadrado e a estação meteorológica. O método do metro quadrado provou ser uma ferramenta melhor para medir as intensidades de chuva. Além disto, o vento, quando em condições mais fortes, têm uma influência notável na geração da chuva sintética. Observam-se tendências semelhantes nos resultados da comparação entre a chuva sintética e o modelo teórico, com curvas decrescentes e picos crescentes à medida que a intensidade da chuva aumenta. O pico da distribuição Marshall-Palmer está em 10^4 gotas, enquanto os picos da distribuição de gota da chuva sintética estão mais próximos de 10^3. Assim, é digno de nota que hà a necessidade de aumentar o número de gotas em todos os tamanhos de diâmetro para a chuva sintética. Embora o número de gotas e o formato das curvas sejam diferentes, o que se justifica pelo fato de um ser experimental e o outro um modelo matemático, os padrões observados alinham-se, sugerindo que a chuva artificial se assemelha ao modelo teórico. A comparação entre DSDs de chuva sintética interna e externa, demonstram que a chuva gerada neste trabalho se assemelha melhor às características da chuva real do que a chuva sintética interna. A comparação entre as curvas de chuva sintética e os dados de chuva real fornece uma validação convincente do sistema de geração de chuva, em que, para as três intensidades, as curvas têm uma forma semelhante, indicando que a chuva sintética parece com as características da chuva real em termos de distribuição do tamanho das gotas. Além disso, é observado que maiores intensidades de chuva correspondem a maiores volumes de água, consistente com as expectativas e confirmando a precisão do sistema de geração de chuva na simulação de diferentes níveis de precipitação. Os resultados do RSME obtidos pela comparação das curvas da chuva real com as geradas no CARISSMA, mostram que a curva de 10 mm/h exibe a maior semelhança com a chuva real. É importante ressaltar que os valores de RSME correspondentes são relativamente pequenos, considerando que todas as intensidades permanecem em uma ordem de grandeza semelhante para o número de gotas. Isso ressalta a eficácia do método de geração de chuva sintética proposto nos três níveis de intensidade. O impacto da chuva no desempenho dos algoritmos de percepção dos sensores das câmaras é evidente ao longo da análise. Os resultados experimentais apresentaram degradação sob diferentes intensidades de chuva, mostrando desafios significativos na detecção de objectos. Em contrapartida, o algoritmo apresentou bons resultados de detecção quando exposto a diferentes posições, ou seja, ele detecta o alvo independentemente de sua posição. Assim, conclui-se que o problema do algoritmo sob chuva não é a detecção de objectos, mas a classificação dos mesmos. Também, é evidente que a luz é um parâmetro que deve ser levado em consideração. Houve interferência da luz nas imagens o que introduziu falsos positivos. Estes resultados ressaltam a importância de desenvolver algoritmos de percepção robustos, capazes de lidar com condições meteorológicas adversas, para a utilização segura de veículos automatizados.

CONSIDERAÇÕES FINAIS

A pesquisa destaca a importância de testes em campo para o avanço do desenvolvimento de veículos automatizados. Para viabilizar a confiabilidade desses sistemas em condições meteorológicas adversas, discute-se a necessidade de soluções climáticas sintéticas, oferecendo reprodutibilidade e eficiência. A principal contribuição desta dissertação é a validação de uma chuva sintética externa para ser utilizada em testes automotivos, tornando-se uma alternativa acessível e versátil para múltiplos locais. A geração da chuva sintética abrangeu três intensidades distintas - 10,mm/h, 25,mm/h e 50,mm/h - na instalação de testes do CARISSMA, Alemanha. É evidente a influência significativa do vento nas medições, mas concluiu-se com os métodos de validação que a chuva sintética se aproxima com a chuva real. A análise dos sensores revelou desafios na detecção de objetos em condições de chuva, em que o algoritmo de detecção apresentou problemas na classificação precisa dos objetos. Os testes, também, evidenciaram o impacto da luz na funcionalidade da câmera, destacando a necessidade de medir a quantidade de luz na instalação de teste e ponderar a posição do sol como um fator. As considerações para trabalhos futuros incluem, a introdução de gotas de chuva maiores no sistema de chuva sintética, a mitigação dos efeitos do vento em instalações externas, análise de melhores equipamentos para medir as características do vento, aprimoramentos na detecção de classes de objetos, investigação do intervalo de luz necessário para testes eficazes e a potencial utilização de chuva artificial em redes neurais para treinamento.

Palavras-chave: Chuva Artificial. Teste & Validação. Sensores de Percepção. Veículos Automatizados.

ABSTRACT

This dissertation is focused on the area of developing perception systems for automated driving applications, a critical research to ensure the safety and efficiency of autonomous vehicles. Perception systems rely on the accuracy of the perception sensors and algorithms, which require rigorous testing, especially in adverse weather conditions such as rain, fog, and snow. Therefore, the main objective of this work is to develop and validate an outdoor synthetic rain facility to assist in the testing of environmental perception systems under rain conditions. The methodology proposes the generation of three different synthetic rain intensities, that are validated by comparison with real rain data, a theoretical rain model, and synthetic rain data generated indoors. This validation process involves several parameters, including data from a disdrometer and a meteorological station. The synthetic rain exhibited satisfactory uniformity within the test area, effectively replicating the three intended levels of rainfall intensity. Additionally, it was observed that wind can influence the outdoor generation process. When compared with real rain data and a theoretical model, the results obtained demonstrated similar patterns. Subsequently, external synthetic rain showed greater similarity to real rain when compared to internal synthetic rain, proving to be a viable, controlled, and reproducible test method. In addition, this system allows for reliable data collection in adverse weather conditions. Consequently, a case study was conducted with a camera using artificial intelligence techniques for object detection to compare the algorithm's performance in rainy and non-rainy weather conditions. It was observed that the object detection results under synthetic rain were inferior, causing the algorithm to misclassify objects. In this case, it detects a boat instead of a car. Further analysis shows that the illumination in the images is a significant factor influencing the results, highlighting the importance of this aspect for future testing. The results of this work contribute to the understanding of the impact of rain on the perception capabilities of the algorithm, which is a fundamental step towards ensuring the safety of autonomous vehicles in adverse weather conditions.

Keywords: Synthetic Rain. Test & Validation. Perception Sensors. Automated Driving.

LIST OF FIGURES

LIST OF TABLES

LIST OF ABBREVIATIONS

ADS	Autonomous Driving Systems
AI	Artificial intelligence
AP	Average Precisions
AVs	Automated Vehicles
C-IAD	CARISSMA - Institute Automated Driving
CNNs	Convolutional Neural Networks
DSD	Rain Drop Size Distribution
EM	Electromagnetic
EPS	Environmental Perception System
FN	False Negatives
FP	False Positives
GPS	Global Positioning System
IoU	Intersection over Union
Lidar	Light Detection and Ranging
mAP	Mean Average Precision
MEMS	Micro Electro-mechanical systems
Radar	Radio Detection and Ranging
RGB	Red, Green and Blue Wavelengths
RMSE	Root Mean Square Error
R-CNN	Region-based CNN
RTK	Real-Time Kinematic
SAE	International Society of Automotive Engineers
THI	Technische Hochschule of Ingolstadt
TN	True Negatives
TOF	Time-of-Flight

TP	True Positives
YOLO	You Only Look Once
XiL	X-in-the-Loop

LIST OF SYMBOLS

A	Slope parameter
a	Area
D	Diameter
m	Weight
$N(D)$	Concentration of raindrops
N_0	Intercept parameter
n	Number of diameter classes
O_i	Quantity of drop per diameter real
R	Rain intensity
r	Radium
S_i	Quantity of drop per diameter
t	Time
V	Volume
ρ	Density of water
π	Pi

CONTENTS

1 INTRODUCTION

Vision Zero, the European Commission's strategy to eliminate all traffic fatalities and severe injuries by 2050 while increasing safe, healthy and equitable mobility for all (European Commission, 2019), has been a catalyst for prioritizing Automated Vehicles (AVs). This commitment to AV innovation is exemplified by collaborative efforts such as the Automated Driving Applications and Technologies for Intelligent Vehicles (AdaptIVe). Launched in 2014, the project brings together equipment manufacturers, automotive suppliers, research institutes, and companies, all united by the common goal of improving the safety and efficiency of automated driving (CORDIS EU research results, 2017). By actively participating in such initiatives and being known for its automotive prowess, Germany has embraced this vision and made AV development a focal point within its automotive industry and government (German Association of the Automotive Industry, 2022).

This technological revolution represents a breakthrough in transportation, driven by the vision to improve road safety, reduce traffic congestion, increase mobility accessibility and achieve energy savings (Brown et al., 2014; Folsom, 2012; Morrow et al., 2014). In contrast, many challenges remain, including legal liability concerns in the event of accidents, cybersecurity, system failure risks, personal data protection, ethical concerns, and the need to establish a global regulatory framework for driverless cars (Frisoni et al., 2016).

Afterward, with the advance of AVs, the burden of ensuring safety increasingly shifts from the driver to the system itself. The transition empowers Artificial Intelligence (AI) algorithms embedded in the vehicles to perceive the surroundings, make appropriate decisions, and maintain a safe driving environment. Consequently, the demand for reliable surround sensor systems, highly robust and real-time capability, grows (Cui et al., 2022). The purpose of these sensors is to identify potential obstacles, including other vehicles, pedestrians and various obstructions. Cameras, Radio Detection and Ranging (Radar) and Light Detection and Ranging (Lidar) are mainly involved in environment perception and are heavily studied for the development of Automated Driving Systems (ADS). These systems are designed to reduce the occurrence of accidents and provide maximum protection for both vehicle occupants and road users.

Rainfall has been identified as a significant contributor to road accidents, leading to an alarming increase of up to 70% in reported incidents during adverse weather conditions (Cui et al., 2022). In addition, Sezgin et al. (2023) confirms that there is a loss of sensor performance in rain situations. This highlights the importance of evaluating the reliability of perception sensors in a variety of environmental scenarios prior to market introduction. Therefore, evaluations should include not only standard road conditions but also challenging situations involving the presence of rain, snow, and fog. Consequently, there is a corresponding increase in the demand for rigorous testing and validation of ADS (Stellet et al., 2015).

Field tests have proven to be a valuable evaluation method. These experiments take place in real-world controlled environments that allow the study of naturalistic driving behavior.

For instance, Figure 1 shows a test case of perception surround sensors implemented in a BMW M8 car model conducted at the CARISSMA outdoor facility in normal weather terms. However, for adverse weather testing, controlled weather conditions are not directly available in natural environments and often require several months of data collection. So, there is an important need to create synthetic weather solutions for data collection and real-world testing. This approach has numerous benefits: it enables reproducible data creation, increases time efficiency, improves control, faster access to results, and greater adaptability (Meyer, 2017).

Figure 1 – Field test in CARISSMA outdoor facility

Source: Author (2023)

Numerous studies are using artificial rain, such as Hasirlioglu et al. (2016a) that shows the construction of a mobile rain simulator with a watering area of $2.2\,\text{m} \times 4\,\text{m}$, or in Hasirlioglu (2020), which discusses indoor rain methods and distribution. For synthetic fog, Jokela et al. (2019) and Li et al. (2021) perform perception sensor tests and analyses in artificial fog. It is noticed that most works on synthetic weather generation are performed in indoor controllable environments which require higher financial investments for the construction of the test surroundings.

In order to address this limitation, this work presents a methodology for generating synthetic rain in an outdoor test facility and uses artificial intelligence techniques of object detection to compare perception algorithms in rainy and dry weather conditions. The contribution of this dissertation lies in the validation of an artificial rain system, which can be applied in various facilities, offering accessibility and cost-effectiveness compared to constructing indoor systems. This corroborates to the reduction of real-world testing while ensuring safety, enhancing repeatability and accelerating the data generation for AI algorithms applied to ADS. Furthermore, the results of this project can significantly contribute to the understanding of the effects of rain on sensor perception, and thus to the optimization of these systems for AVs.

1.1 OBJECTIVE

The primary objective of this work is to develop and validate an outdoor synthetic rain facility to perform proving ground testing of automated driving systems.

The specific objectives of this work are:

- Define the mobile system required for the generation of rain on an outdoor proving ground;
- Specify the system arrangement for generating different intensities of synthetic rain;
- Validate the different rain intensities to achieve a realistic distribution of raindrops;
- Identify the influence of rain conditions on the perception system of AVs.

1.2 OUTLINE

This dissertation is structured into four distinct chapters. The first chapter provides a comprehensive literature review, that delves into the concepts related to this research, including automated driving vehicles, perception sensors, adverse weather conditions and a state-of-the-art review on the impact of adverse weather on ADS. The subsequent chapter outlines the methodology. The materials and methods used to generate the outdoor rain are introduced and the methodology for validating it is discussed. The second part focuses on sensor data acquisition, algorithm usage, and evaluation techniques. This is followed by a chapter dedicated to the analysis of the results, which discusses the main outcomes and is also divided into two parts: one for the rain discussion and the other for analyses of the sensor data. The final chapter presents the conclusion, which compares the results and highlights potential directions for future research.

2 LITERATURE REVIEW

In the current scenario, the pursuit of automated vehicles has stimulated interest and innovation. This chapter provides fundamental aspects of automated driving, focusing on its core functionalities and the critical role of its perception sensors. Subsequently, the impact of adverse weather conditions on the AVs are explored, with an overview of the current state of research and test methodologies in this area.

2.1 THE EVOLUTION OF AUTOMATED DRIVING

Automated vehicles, often referred to as self-driving vehicles, represent a technological advancement in the realm of transportation. These motor vehicles, which include cars, trucks, and buses, are equipped with technology designed to assist the driver and facilitate the transfer of driving functions from a human operator to a computer system (Pillath, 2016). Its development has a rich history dating back to the 1920s when initial experiments were conducted and Figure 2 shows a visual timeline representation of the technical evolution.

Figure 2 – Timeline of automated vehicles evolution

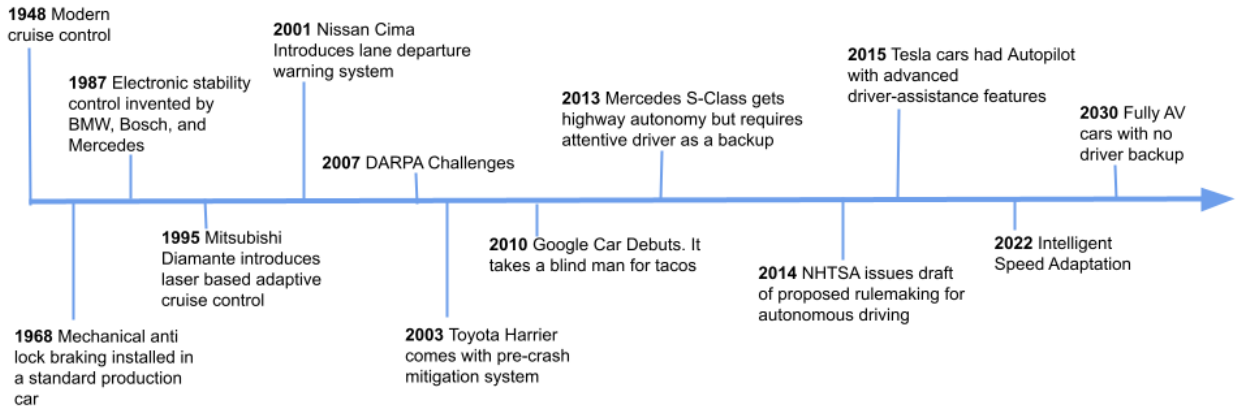

Source: Adapted from Ondruš et al. (2020)

Significant progress was made in the 1950s, with Japan playing a pioneering role in this field, and eventually, various countries, including Germany, Italy, and the United States, joined the effort (Greenblatt; Shaheen, 2015). Notably, autonomy in vehicles began to take shape in the 1980s with the EUREKA Prometheus Project initiated by Mercedes-Benz and the University of Bundeswehr Munich (Ondruš et al., 2020). The 2000s brought about significant advances in AV technology, with the introduction of key features such as the lane departure warning system and autopilot functionality introduced in Tesla Motors vehicles in 2015 (Ondruš et al., 2020). In 2022, certain car models were introduced with intelligent speed adaptation for usage on the road, and it is predicted that fully autonomous vehicles are expected to reach the market by 2030 (Europian Parliament, 2019).

To facilitate a clearer understanding of AVs, the International Society of Automotive Engineers (SAE) has established a classification system that categorizes different levels of automation (Society of Automotive Engineers, 2021). Figure 3 provides a visual representation of these levels.

Figure 3 – Levels of driving automation

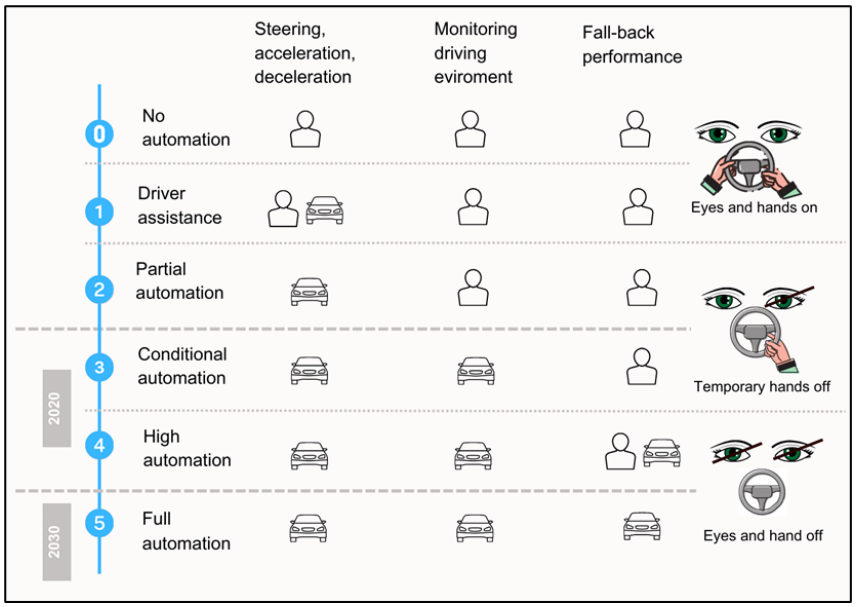

Source: Author (2023)

In essence, the system delineates how the responsibilities of the driving task are distributed between the human driver and the machine. The levels are categorized bellow.

- Level 0: denotes the initial standard features found in a car with no technical awareness to detect objects or warnings;
- Level 1: autonomy stands for vehicles equipped with basic sensors that can provide warnings (visual or audible) and partially detect dangerous situations;
- Level 2: means that the car is able to reproduce a current situation or use a case in a machine-interpretable way. Upon request, it can and will engage in a decision-making process. However, the driver retains the ability to take control and must monitor the car at all times;
- Level 3: implies the introduction of a responsibility shift, as the vehicle could at times take over the driving task. The machine can automatically assess when driver intervention is needed and request it accordingly;
- Level 4: the car will do most of the driving itself, with the driver having the option to take the wheel only when requested. However, the vehicle should be able to assume full driving responsibility throughout the trip and its usage is confined to some specific locations;

- Level 5: means fully driverless cars with no steering wheel or other features that allow human control.

In alignment with the European Parliament's directives, Level 3 automation has been integrated into autonomous vehicles since 2020 and the development process for a truly autonomous vehicle, Level 5, has not yet reached the stages of design, extensive testing, manufacturing, regulatory approval, pricing, or marketing. Each level presents unique challenges in terms of sensor accuracy, decision-making algorithms, and human-vehicle interaction. These challenges require cutting-edge technology because, as mentioned before, they essentially replace human decision-making with computer algorithms. Especially at Level 3 and above, the technology to enable automation is extremely sophisticated and very expensive. For efficient development, it is essential to break the entire task into smaller and more manageable modules, known as functional system architecture. The next section explains the details of this design and development architecture for advanced autonomous driving systems.

2.2 THE AVS FUNCTIONAL SYSTEM ARCHITECTURE

The system architecture allows a structured decomposition of the functionality into discrete modules, each responsible for specific aspects, with the goal of the vehicle to make its own decisions by sensing the environment and controlling the mobility of the vehicle (Zong et al., 2018). According to Ahangar et al. (2021), the architecture is composed of four main stages, as seen in Figure 4.

Figure 4 – System architecture for AVs

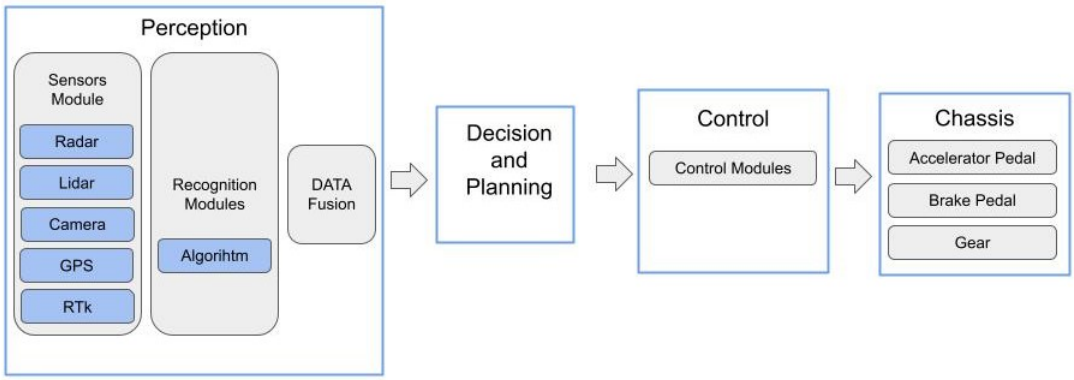

Source: Adapted from (Ahangar et al., 2021)

The first stage, Perception, is the sensing of the AV's environment through an array of sensors usually classified into two classes: internal state sensors and external state sensors. The first captures the dynamical state variables, measuring internal values of the dynamic system and its own position relative to the environment, including sensors such as Global Positioning System (GPS) and Real-Time Kinematic (RTK). In contrast, the external state sensors perceive and gather information external to the system. Cameras, Radar and LiDAR

are examples of external state sensors. Within this stage, the data collected by these sensors is processed by algorithms. This processed information is then integrated and forwarded to the subsequent stage. In the Decision and Planning stage, the AV uses the data collected during the perception process to make informed decisions and formulate plans about its motion and behavior. The output of this stage is a set of well-informed instructions to the control module, which performs physical control actions, including steering, braking, and acceleration. The final stage, Chassis, activates the mechanical components attached to the AV's chassis, such as the brake pedal motor, steering wheel motor, and powertrain.

In summary, the machine processes environmental perception data through the use of advanced algorithms, resulting in outputs that inform decision-making and subsequent action execution. As a result, the vehicle's onboard computer is able to interpret complex traffic dynamics, recognize road signs, identify obstacles, and track pedestrian movements. This assimilation of inputs enables the vehicle to make well-informed decisions, that dictate its path, regulate its speed, and orchestrate interactions with its environment (Titu et al., 2020).

This dissertation focuses on the first stage of the functional system architecture, the Environmental Perception System (EPS), and as already mentioned, its main task is to collect and interpret data about the environment to enable the vehicle to perceive its surroundings. The EPS works by integrating data from several strategically placed sensors on the vehicle, which are devices that translate the detected events or changes in the environment into a quantitative measurement for further processing by the perception algorithms (Ahangar et al., 2021). The primary sensors, including camera, lidar, and radar, are strategically distributed across various sections of an automated vehicle, as shown in Figure 5 which according to Titu et al. (2020) is a typical placement of these sensors in an automated car.

Figure 5 – Model representation of the placement of sensors in AVs

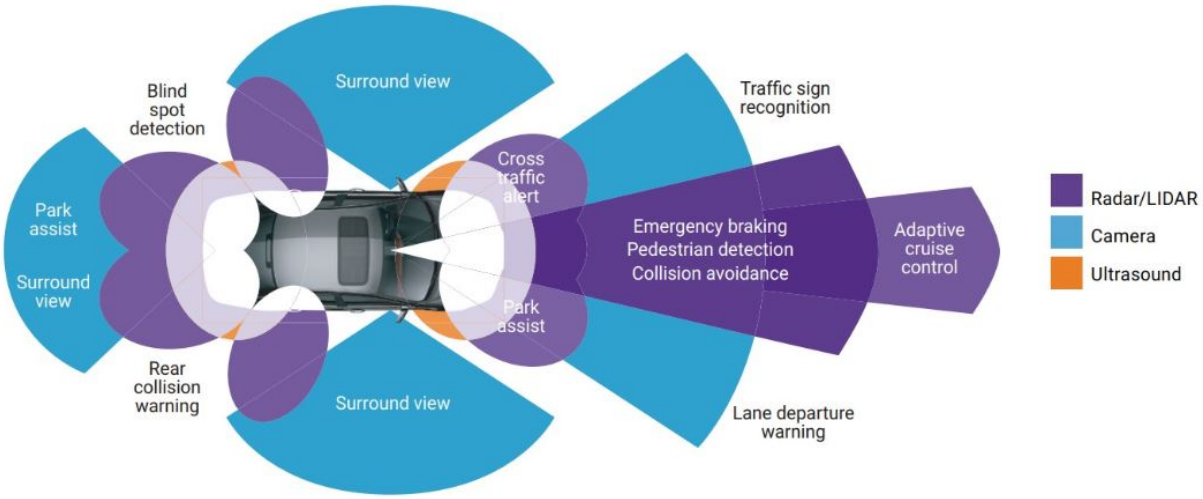

Source: (Titu et al., 2020)

It can be noted that the sensors are distributed around the car, ensuring comprehensive coverage of the vehicle's surroundings, and addressing the need to capture data from all perspectives. In particular, it is challenging to generate adequate information from a single independent sensor source (Yeong et al., 2021). Therefore, once data is collected from these sensors, it undergoes a process called sensor fusion. Sensor fusion involves combining information from multiple sensors to improve the accuracy and reliability of the environmental sensing system, and several reviews have recently been published on the topic of multi-sensor fusion (Velasco-Hernandez et al., 2020), (Campbell et al., 2018). The following section discusses the characteristics, advantages, disadvantages, and respective roles of the primary sensors. The idea is to gain an in-depth understanding of each sensor's functionality individually, with the goal of optimizing them.

2.3 PERCEPTION SENSORS

According to Rawat (2019), perception sensors can be categorized into two primary types: active sensors and passive sensors. Active sensors operate by emitting their own energy into the surrounding environment and subsequently measuring the reaction of the environment itself. Conversely, passive sensors do not emit energy but rather measure the ambient environmental energy that naturally enters the sensor. This section reviews the functionality, advantages and limitations of the three primary sensors for environment perception in automated driving applications.

Radio Detection and Ranging, an active sensor commonly known as Radar, operates on the principle of emitting Electromagnetic (EM) waves into a designated area of interest and subsequently receiving the scattered waves and reflections, from various targets within that area (Rosique et al., 2019). Figure 6 presents a model of an imaging radar.

Figure 6 – Imaging radar model

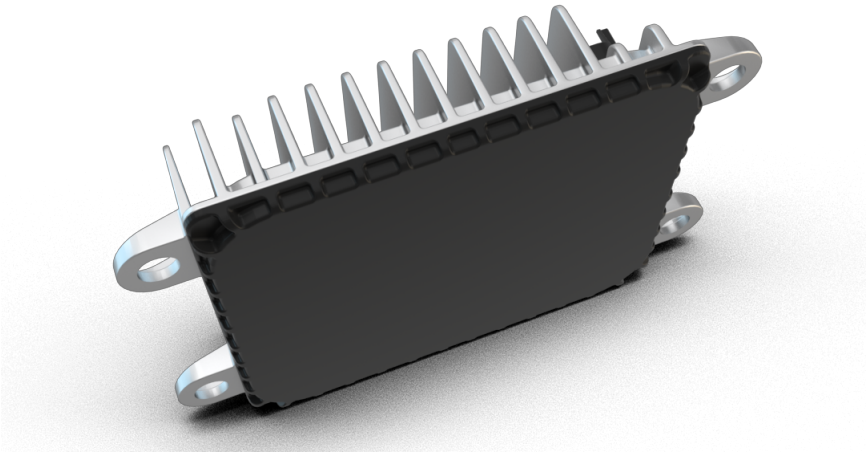

Source: (ZF Press, 2021)

According to Buller et al. (2018), radar sensors exhibit robust performance in various weather conditions and low-light scenarios, in other words, good performance at night. They have a remarkable ability to accurately detect near and far targets. Depending on the placement of the radar, it can detect targets in front of, alongside and behind a vehicle. The disadvantages include inaccurate object detection and classification, especially in scenarios with multiple reflections and a limited Field of View (FOV) (Gini, 2021).

This device uses the Doppler effect (Skolnik, 2008), a fundamental property of EM waves, to determine the relative speed and position of detected objects. According to Skolnik (2008), this phenomenon refers to the change in frequency observed in EM waves due to relative motion between the radar system, the source of the waves, and the objects it detects. It has a good use to distinguish stationary targets from moving ones. Rosique et al. (2019) explains that these received signals undergo complex signal processing techniques to extract valuable information about the range and characteristics of the targets and an example of the radar output is shown in Figure 7.

Figure 7 – Example radar point cloud data

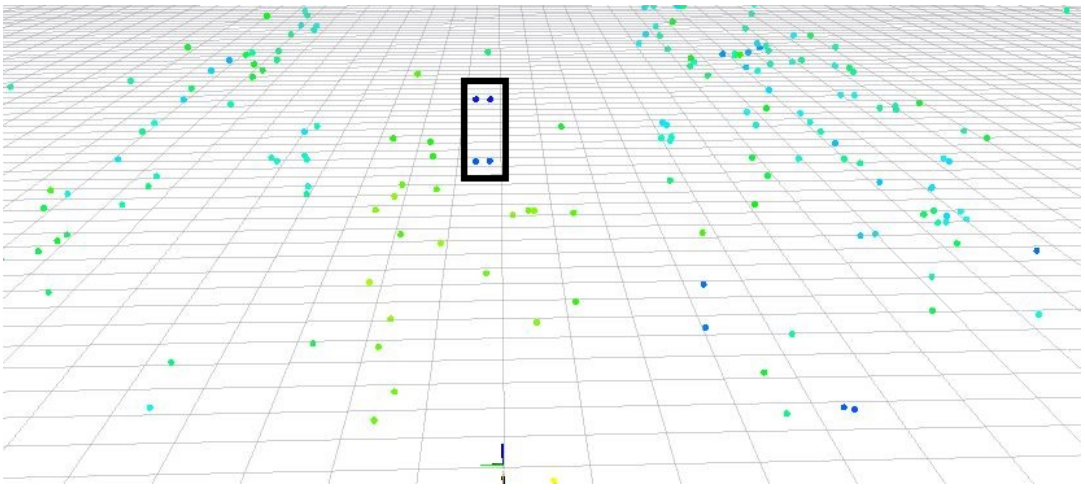

Source: Author (2023)

The output is a 3D point cloud that represents spatial information of the environment surrounding the vehicle, with each point representing a detected object or feature. In this particular example, the positioning of the vehicle can be visualized by referencing the black rectangle in Figure 7. The processing of the data is therefore critical, as it enables the identification of the points that distinguish between vehicles, pedestrians, buildings and road infrastructures.

Light Detection and Ranging, or Lidar, is an active sensor that casts light on its surroundings by emitting a laser, which is reflected by target objects (Li; Ibanez-Guzman, 2020). These reflections are detected by the instrument, and the time interval between the emission and reception of the light pulse is used to calculate the distance, the Time-of-Flight (TOF) principle (Campbell et al., 2018). These are complex devices, that can provide full $360°$ visibility of the environment, as the model presented in Figure 8, and there is much potential to be explored in future research.

Figure 8 – 360° lidar model

Source: (Ouster, 2023)

As the lidar scans its surroundings, the end result is a point cloud of precise elevation points that are accurately referenced to the global geocentric system (Saraf et al., 2014). This produces a three-dimensional representation of the scene with greater range and depth perception, as shown in Figure 9 with the colors referencing the intensity of the reflected signal. The limitations include the lack of object color information and the system is not as proficient in object classification as camera systems.

Figure 9 – Example lidar point cloud data

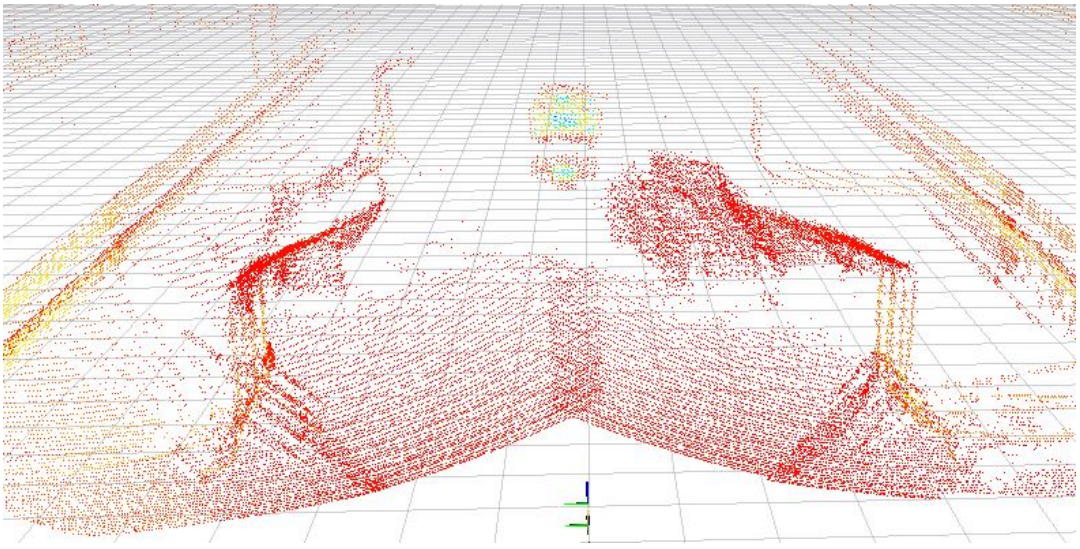

Source: Author (2023)

Unlike radar and lidar, which are active sensors, camera sensors are passive devices that rely on external light sources, which may include sunlight during the day or artificial light from vehicles and street lights at night. Therefore, the camera principle is to detect the emitted light and produce high-resolution images of the surroundings (Yeong et al., 2021). As a result, they are highly dependent on environmental and lighting conditions.

In AVs, there are two types of cameras: monocular or binocular. The first, consists of a single camera to deliver a series of images and the more conventional is the Red, Green and Blue Wavelengths (RGB). The second, also known as stereo cameras, consist of two image sensors that are separated by a baseline, as 3D cameras (Orbbec, 2020). The baseline, which denotes the distance between the two image sensors, varies depending on the specific model of the camera and the benefit is that the distance of the targets can be estimated by comparing both images.

The camera, shown in Figure 10, consists of a 2D array of RGB pixels that detects the light reflected from various surfaces in the environment and converts it into a digital signal (Schlager et al., 2020). The camera captures the 3D environment and projects it onto a 2D plane, so the output is image frames. It accurately displays the contour, texture, color distribution, and other information of the object from a certain angle (Wang et al., 2020).

Figure 10 – RGB camera model

Source: (LUCID Vision Labs, 2023)

2.4 PERCEPTION ALGORITHMS: CAMERA DATA

The goal of perception algorithms is to convert sensor data into lists of objects, essentially performing object detection. The output of this process includes the positions of these objects, which are used in the decision-making phase of the functional system architecture. In the context of camera-based object detection algorithms, the central objective is to define bounding boxes around objects identified within an image (Hasirlioglu, 2020). These bounding boxes include the dimensions and spatial coordinates of the objects and are often linked to an object category. In addition, they contain a confidence score that indicates the probability that the bounding box encloses an object of the specified category. The most common approach to object detection is the adoption of Convolutional Neural Networks (CNNs). Networks, in artificial intelligence, refer to interconnected layers of computational nodes that process input data. Krizhevsky et al. (2012) affirms that CNNs are characterized by significantly fewer con-

nections and parameters in comparison to standard feed-forward neural networks. These CNNs have demonstrated superior accuracy in object recognition tasks, making them easier to train.

Prominent models in this domain include the R-CNN family, which involves the use of two separate neural subnetworks — one for detection and another for classification (Girshick, 2015). However, this dual-network approach often results in slower processing speeds, making them less suitable for real-time applications in automotive systems. In contrast, YOLO (You Only Look Once) operates as a single-stage detector, that simultaneously predicts multiple bounding boxes and associated object probabilities from a single neural network (Du, 2018). Given YOLO's exceptional execution speed and its ability to identify multiple objects within the same image and with different classes, it is the algorithm used in this work, more specifically the version 7 (Wang et al., 2022) that was released in 2022. An example of an object detection application is shown in Figure 11.

Figure 11 – YOLO object detection

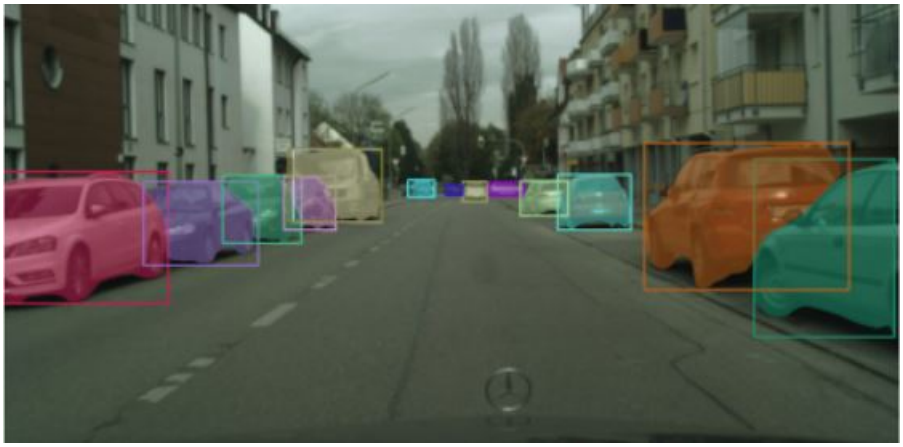

Source: (Wang et al., 2022)

2.5 INFLUENCE OF ADVERSE WEATHER ON PERCEPTION SENSORS

The impact of adverse weather conditions, including rain, snow, fog and light, poses a challenge to the reliability and accuracy of perception systems. These climatic variables give rise to complications that require examination for the safety and efficient navigation of self-driving vehicles. In the existing literature, it is possible to find reviews that focus on the evaluation of the performance of common sensors utilized in AVs under various weather conditions (Zang et al., 2019),(Kutila et al., 2018), (Brophy et al., 2023). Zang et al. (2019) focuses on the effect of rainfall on radar and confirms that heavy rain can reduce the detection range of the radar waves by up to 45%. Kutila et al. (2018) observed that with adverse weather conditions, the performance of the Lidar has a 50% reduction in target detection. Brophy et al. (2023) explore which adverse weather conditions impact the performance of cameras. An interesting analysis is introduced by Zhang et al. (2023), which presents a state of the art of the impact caused by weather conditions on perception sensors, and an overview is presented in Table 1.

Table 1 – Influence level of weather conditions on sensors. The numbers represent a risk scale: 0 - negligible, 1 - minor, 2 - slight, 3 - moderate, 4 - serious, 5 - severe

Modality	**Light rain**	**Strong rain**	**Fog**	**Snow**	**Strong light**
Lidar	2	3	4	5	2
Radar	0	1	0	2	0
Camera	3	4	4	2	5

Source: Adapted from (Zhang et al., 2023)

The level of impact of each phenomenon on sensors is rated on a scale from 0 to 5. A rating of 0 indicates negligible effects that can almost be ignored. A rating of 1 is a minor effect that will barely cause a detection error. A rating of 2 represents minor influences that cause small errors on specific occasions. A rating of 3 suggests moderate influences that cause perception errors up to 30% of the time. A rating of 4 points for serious influences that cause perception errors more than 30% but less than 50% of the time. Finally, a rating of 5 categorizes severe influences, including noise or blockage, that lead to false detections or detection failures. As can be noticed in the table, radar is the less affected sensor. For lidar, raindrops and snowflakes can scatter sensor signals, degrading data quality and causing inaccuracies in distance measurements and object detection. Similarly, with a risk scale of 4 for fog, the particles in the atmosphere also scatter signals and absorb energy, further complicating obstacle detection. Thus, these weather conditions cause sensor interference and signal degradation (Vriesman et al., 2020).

In the camera study, almost all the indices of the risk scale are greater than 2. Therefore, Zhang et al. (2023) shows that snowfall can occasionally obscure the sensor's view by depositing flakes in the sensor field of view, potentially leading to false object detection. Fog reduces visibility, making it difficult for the camera to provide an accurate representation of the environment. Rain can also obscure the field of view, as can be seen as an example in Figure 12.

Figure 12 – Contamination effect on a car backup camera

(a) Normal backup image (b) Camera lens soiled by mud (c) Soiled backup image

Source: (Zhang et al., 2023)

Contamination in the camera is naturally formed during road driving after rain, resulting in poor image quality and reduced detection range. Similarly, strong light, such as intense sunlight, severely affects (risk scale equals to 5) the performance of the camera sensor by causing overexposure in captured images, resulting in the loss of critical visual information. It is evident that there are many challenges, especially for cameras.

Overcoming these difficulties is fundamental to the development of autonomous vehicles. The following sections discuss methods and tests aimed at mitigating these complexities, as well as state of the art solutions for improving perception systems and ensuring the reliability of autonomous vehicles in the face of adverse weather conditions.

2.6 TEST METHODOLOGIES AND VALIDATION UNDER WEATHER CONDITIONS

A variety of testing methods are employed to ensure safe and reliable operation, encompassing virtual-world testing, X-in-the-Loop (XiL) simulations, real-world testing, and proving ground evaluations. Virtual-world testing uses computer simulations to assess vehicle performance in various scenarios, while XiL uses a combination of real and simulated components, where X refers to anything under test interacting in a loop with the environment model. It can be a model, software, hardware, or the whole vehicle. Real-world testing involves conducting tests on actual roadways and proving ground evaluations are performed in controlled and repeatable settings, which are ideal for testing and validating the entire vehicle behavior in different scenarios (Huang et al., 2016).

These different test methods address the many requirements of developing a safe automated vehicle, each with its own advantages and disadvantages. To achieve a high degree of realism in XiL and virtual world testing, the integration of models capable of simulating sensor-specific effects is critical, and the inclusion of real-world data inputs is essential. Subsequently, real-world testing provides naturalistic settings and exposure to unpredictable external factors, but, it can be expensive, time-consuming, and have limited repeatability.

When researching the impact of weather conditions on AVs, it's important to recognize the sporadic and location-dependent nature of weather patterns. For example, regions with tropical climates rarely experience snowfall, making snow testing impractical. In addition, natural rainfall is unpredictable and may not provide a consistent and persistent environment for experimental data collection, as the experiment must run for an extended period of time to collect sufficient data under adverse meteorological conditions (Benmimoun et al., 2013). To address these limitations, proving grounds testing emerges as a solution, offering controlled and reproducible environments for testing. Facilities equipped with synthetic weather systems can provide nearly identical environmental conditions to the real world.

For instance, Figure 13 shows the test center CARISSMA, an indoor proving ground with a lane of $123\,\mathrm{m}$ long building, located in Ingolstadt, Germany. This facility is capable of producing synthetic fog and rain with a maximum rain intensity of $98\,\mathrm{mm/h}$. At the top of the picture, the nozzles used to spray water can be seen.

Figure 13 – CARISSMA indoor test center

Source: (Sezgin et al., 2023)

Other notable test facilities with various capabilities for autonomous vehicle proving grounds are documented in the work of Zhang et al. (2023). Table 2 provides a detailed overview of the facilities.

Table 2 – Experimental weather facilities across the world.

Experimental facilities	**Rain**	**Fog**	**Snow**	**Light**	**Country**	**Lenght**
JARI proving ground	✓	✓	-	✓	Japan	200 m
VTTI Smart roads	✓	✓	✓	✓	USA	800 m
DENSO	✓	-	-	✓	Japan	200 m
Center for road weather proving ground	✓	✓	✓	✓	Korea	600 m
CEREMA climatic chamber	✓	✓	-	-	France	31 m
NIED environment simulator	✓	✓	-	-	Japan	N/A
CATARC proving ground	✓	✓	✓	✓	China	60 km
CERI Tomakomai test road	-	-	✓	-	Japan	N/A
Sod5G meteorological institute	-	-	✓	✓	Finland	11 km

There are many indoor proving ground options around the world, each with varying weather conditions, with the added benefit of precise control over precipitation rates, light, fog, and snow. This setup also reduces the risks associated with hazardous conditions, making it a safer option compared to real-world testing. Conversely, when delving into the literature review encompassing test sites, the only outdoor rain generation model found is the one referenced in Figure 14. The test approach clearly has a size limitation when comparing the rain structure to the car model in the figure. This disparity in scale is a notable limitation within the test approach, potentially hindering accurate simulations or evaluations.

Figure 14 – Outdoor Ring for rain generation

Source: (Brzozowski; Parczewski, 2023)

Given these facts, this dissertation presents an outdoor synthetic rain generation methodology and applies it in a case study to evaluate its impact on perception cameras. Building on this case study, the work by Brophy et al. (2023) critically evaluates the influence of rain on camera sensors. The author highlights that research in this area is lacking, with limited exploration of various aspects, particularly in relation to image sensors and subsequent processing algorithms on adverse weather conditions. In addition, open sources of adverse weather datasets are currently insufficient to provide comprehensive coverage. While some datasets show a variety of weather conditions, they often don't provide detailed labeling and are not open source, limiting their potential. Collecting more complex weather labels during data collection is essential to gaining a thorough understanding of rain's impact (Brophy et al., 2023).

In summary, rain has far-reaching effects on the autonomous vehicle environment, many of which have not been fully explored and require further research efforts. This reaffirms the importance of this work, as it provides a synthetic rain to be used in datasets of tests in adverse weather conditions, to investigate camera perception algorithms detection.

2.7 RAIN CHARACTERISTICS

Rainfall is a complex and dynamic atmospheric phenomenon, characterized by the presence of individual raindrops with different sizes and falling speeds (Benmimoun et al., 2013). The shape of a raindrop is a dynamic phenomenon. As raindrops fall, they undergo rapid shape changes known as oscillations (Garg; Nayar, 2007). However, for most of the experiments related to vision, the effects of these oscillations are typically negligible. Therefore, Garg and Nayar (2007) explains that it is common to assume that raindrops have a fixed shape, known as their equilibrium shape, which depends on their size, Figure 15. In general, smaller raindrops maintain a spherical shape and as raindrop size increases, they tend to transition to an oblate spheroid shape, flattened in the direction of fall, $\theta = 0$, due to air pressure.

Figure 15 – The shapes of raindrops of various sizes (0.5–2.5 mm)

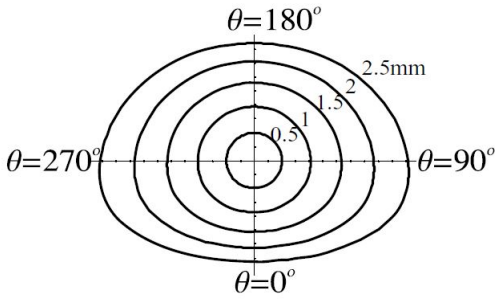

Source: (Garg; Nayar, 2007)

Typically, the mean diameter of raindrops falls within the range of 1 mm and 3 mm, and this mean size tends to increase with higher rain intensity (Meyer, 2017). The range of rain intensities of practical importance generally extends from 12 mm/h to 120 mm/h. In addition, as a raindrop falls, it reaches and maintains a constant speed, known as its terminal velocity, which can vary from 0.1 m/s to more than 9 m/s (Uijlenhoet; Sempere Torres, 2006). This variation in terminal velocity is influenced by factors such as drop size, shape, and air resistance. Smaller raindrops require less height to reach their terminal velocity compared to larger raindrops (Laws; Parsons, 1943).

One of the fundamental attributes that defines rain is the Drop Size Distribution (DSD), which quantifies the number of raindrops within a specific diameter interval per unit of air volume. In the field of meteorology and rain characterization, various drop size distribution models have been developed over the years to accurately represent the distribution of a given rain event, including exponential, gamma, lognormal, and Weibull distributions (Hasirlioglu, 2020). Despite the availability of these different DSD models, the most widely used theoretical distribution in rain research is the one proposed by Marshall and Palmer (1948). It is represented mathematically as

$$N(D) = N_0 e^{-AD}, \tag{1}$$

where $N(D)$ is the concentration of raindrops between D and $D + dD$, N_0 represents the intercept parameter, set as 8000 m^{3}mm^{-1} and A is the slope parameter, characterized by

$$A = 4.1R^{-0.21}, \tag{2}$$

with R being the rain intensity measured in mm/h. Therefore, Marshall and Palmer (1948) proposed a parametrization as a function of rain intensity (R). The range of the drop diameters (D) usually has an interval between 0 mm and 9 mm, where the increment value (dD) depends on the case setup. To exemplify, Figure 16 shows the Marshall-Palmer drop size distribution for a rainfall rate of 30 mm/h.

Figure 16 – Marshall-Palmer DSD model

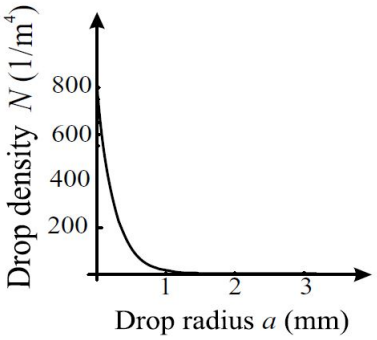

Source: (Garg; Nayar, 2007)

In this case, the diameters ranged from 0 mm to 3 mm, showcasing that smaller raindrops exhibit higher drop concentration, while larger drop sizes correlate with reduced concentration. This graphical example has a diameter parameterization that results in the drop concentration having the unit of $1/\mathrm{m}^4$.

Therefore is important to understand the DSDs and rain intensity levels, and to accurately reproduce them to reliably assess sensor performance in adverse weather conditions. For accurate evaluations using an adverse weather generator, it is essential that the synthetic rain closely resembles real rain, while clearly recognizing its limitations. According to Hasirlioglu (2020), there are several requirements that must be met in order to produce realistic rain:

- Realistic drop sizes and distributions;
- Variable degree of severity, in other words, low/medium/high intensities of rain;
- Constant properties over the segmented area;
- Constant properties over the test duration.

The steps to fulfill the requirements are discussed in the methodologies chapter and for this dissertation, rain intensities less than or equal to 10 mm/h are called low rain. Rain intensities up to 25 mm/h are referred to as medium rain, and rain intensities up to 50 mm/h are high rain. In addition, unlike the parametrized results given by the Marshal-Palmer model, this research uses a device to measure the DSDs that has as output the density of raindrops per m^3. The choice and use of the instrument will be better explained in the next chapter.

3 METHODOLOGY

The Methodology chapter outlines the materials, methods and procedures used in this dissertation. It is divided into two sections. Section 3.1 covers the methodology used to generate the outdoor synthetic rain and the various techniques employed for validation. Section 3.2 delves into the process of sensor data acquisition and the subsequent analysis using artificial intelligence algorithms.

3.1 SYNTHETIC OUTDOOR RAIN

This section proposes the methodology for creating artificial outdoor rain with three different intensities (mm/h). It includes two subsections. The first one deals with the characterization of the test site and the explanation of the equipment used to generate and measure the synthetic rain. This is followed by the second subsection that proposes the validation approach.

3.1.1 Synthetic Outdoor Rain: Generation

The CARISSMA Institute of Automated Driving (C-IAD) outdoor facility, located in Ingolstadt, Germany, is used to generate and validate the outdoor synthetic rain intensity. The infrastructure of the institute, Figure 17, consists of an acceleration zone of $210\,\text{m}$ x $15\,\text{m}$ (delimited by the solid line in the figure) and a dynamic area of $60\,\text{m}$ x $70\,\text{m}$ (bounded by the dashed line in the figure).

Figure 17 – CARISSMA outdoor test facilities, top view

Source: Author (2023)

The generation of the synthetic rain is organized in the acceleration zone. Therefore, garden sprinklers are positioned within the facility, as illustrated in Figure 18. The right image shows the sprinklers in an inactive state, while the left picture shows water flowing from the sprinkler outlets.

Figure 18 – Garden sprinklers placed in CARISSMA outdoor acceleration zone

Source: Author (2023)

A disdrometer, a weather station equipment and the square meter method are used for the rain data collection. The 3D stereo disdrometer from Thies Clima is the instrument used to measure the DSDs of the artificial rain at CARISSMA outdoor. This instrument is composed of a light source and a stereo camera (Thies Clima, 2022), as shown in Figure 19. The particles pass through the measuring volume, $1000\,\mathrm{cm}^3$, which is marked with a circle in the picture, and cause the extinction of the light seen by the cameras.

Figure 19 – Measuting principle Disdrometer This Clima

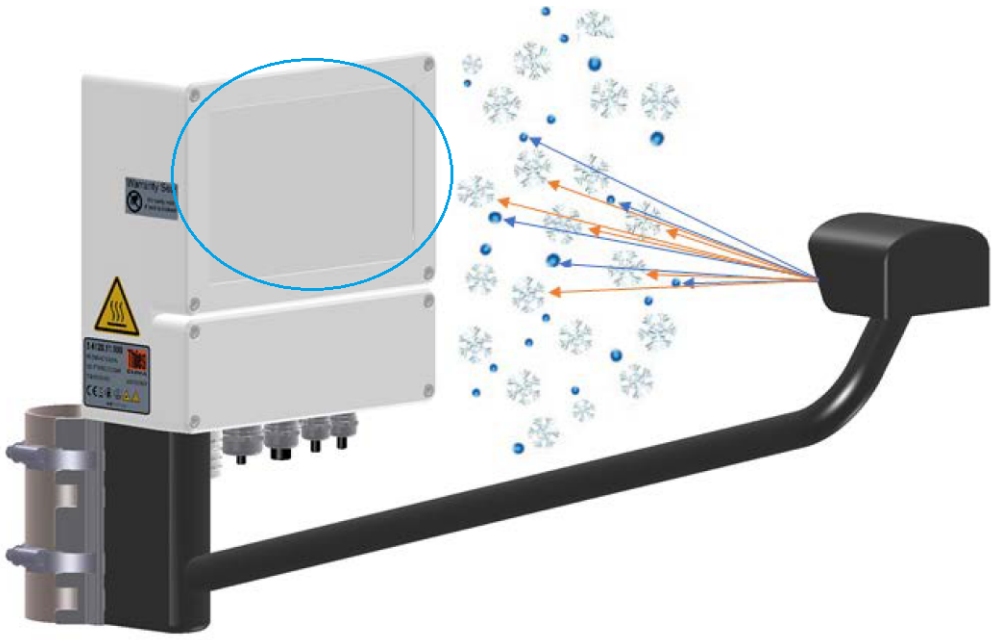

Source: (Thies Clima, 2022)

According to Thies Clima (2022), the sizes of particles are determined by analyzing the area captured by the cameras and their location within the measurement volume. Particle velocities are determined by tracking their movement over a specific time frame. The system utilizes distinctive features in particle images to differentiate between elements such as rain, snow, hail and seeds. Therefore, the output of this device includes number of particles per velocity and per diameter class, total particle size, velocity distribution and rain intensity. The disdrometer is set to divide the drop diameters into 22 classes between 0 mm and 21.6 mm, where the class starts with a variation of 0.2 mm and then increases by 2 after 4 classes.

The WeatherHat, a meteorological station, is equipped with mechanical sensors that operate through physical interaction with the outdoor wind and rain. It utilizes magnets, reed switches, and moving parts to generate signals, which are processed by a Raspberry Pi 4 Model B. These sensors provide measurements for wind speed, wind direction, and rain intensity. For the last variable, the system integrates two interconnected buckets designed to tip upon reaching a predetermined water capacity. This continuous tipping mechanism, where one bucket empties as the other fills, ensures consistent operation during rainfall. Each tipping instance is captured in an electronic record, and using knowledge of the bucket's capacity, the device computes and displays the rain precipitation (Synotronics, 2020).

The disdrometer and the WeatherHat are attached together, along with a waterproof box that encloses the Raspberry Pi, as shown in Figure 20. Data is collected over one minute and transmitted over Ethernet. Code is developed in Python to receive the data from both devices and generate the DSDs as the compilation of Weatherhat data.

Figure 20 – Equipment integration for rain data acquisition

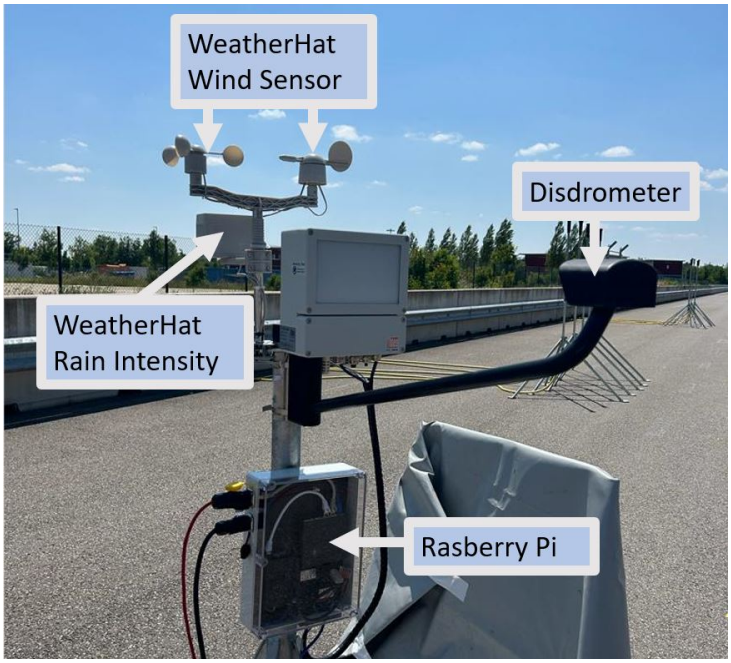

Source: Author (2023)

Alternatively, the square meter method is used to obtain rain intensity from the outdoor synthetic rain generation. It consists of recording the amount of water collected within a predefined time (t) and calculating its volume using the weight (m) and density of water (ρ). Then, using the recipient's surface area (a), the rain intensities can be computed as

$$RainIntensity = \frac{m\rho}{at}. \tag{3}$$

The method involves strategically placing garden sprinklers within the acceleration zone and collecting synthetic outdoor rain data using the specialized equipment described above. This data is used to verify its physical similarity to natural rain, taking into account wind disturbances and performing a comprehensive analysis of the results. The following subsection outlines the study for placing the sprinklers to generate three different rain intensities and details the methods used to validate this synthetic rain.

3.1.2 Synthetic Outdoor Rain: Validation

The collected data is subjected to a comprehensive evaluation, that includes five different analyses that draw comparisons between three distinct experimental environments: the outdoor rain, an indoor synthetic rain, and real-world rain conditions. The purpose of these comparisons is to evaluate the similarity between artificially emulated and authentic rain patterns, while also examining the efficiency of synthetic rain generated under outdoor conditions compared to controlled indoor settings and the theoretical model. Detailed descriptions of each analysis are provided below.

3.1.2.1 Preliminary Analysis of the Sprinklers

To understand the capabilities of the outdoor rain facility and to identify the intensity distribution generated by the different systems, a preliminary test is conducted evaluating the performance of two different garden sprinklers, seen in Figure 21.

Figure 21 – Garden sprinklers model

(a) Spray (b) Rotator

Source: (Hunter Industries, 2023)

The equipment in Figure 21a consists of a spray sprinkler, with a flow rate of $8.90\,\mathrm{L/min}$ and the one in Figure 21b is a rotating sprinkler with a flow rate of $6.88\,\mathrm{L/min}$. Each of these sprinklers covers a semicircular area spanning 180 degrees, with an effective radius of $9\,\mathrm{m}$. The main difference is that the rotating sprinkler has a rotating water jet that scans the area of operation, while the spray sprinkler produces a widespread water jet in its actuation area. For the evaluation, the volumetric amount of water produced by each sprinkler in $30\,\mathrm{min}$ is measured at five distinct positions, as show in Figure 22.

Figure 22 – Evaluation of Sprinkler's performance

Source: Author (2023)

The buckets within the images are arranged in a linear alignment along the zero-degree angle of the sprinkler radius, spaced at $1.8\,\mathrm{m}$ intervals. The value of the volumetric amount of water at the five positions is used to calculate the average rain intensity for the sprinklers with the square meter method. The results and the final choice of equipment are presented in the next chapter.

3.1.2.2 Synthetic Outdoor Rain

Using the available sprinkler constraints defined in the preliminary test, it is possible to estimate the rain capabilities for the CARISSMA outdoor test. As mentioned in Section 2.7, the validation of a synthetic rain requires different levels of rain intensity, so three nominal intensities were chosen to reproduce: $10\,\mathrm{mm/h}$, $25\,\mathrm{mm/h}$ and $50\,\mathrm{mm/h}$, representing low, medium and high rain respectively. Given the availability of 20 sprinklers, their average rain intensity, and the effective radius of each sprinkler, the arrangement is designed to achieve the desired rain intensities in a homogeneous distribution. Figure 23 presents the design analysis for the three nominal rain intensities. The orange dots represent the rotator sprinklers while the half circle illustrates the water dispersion over the 180 degrees.

Figure 23 – Study of the sprinkler position for the rain intensities

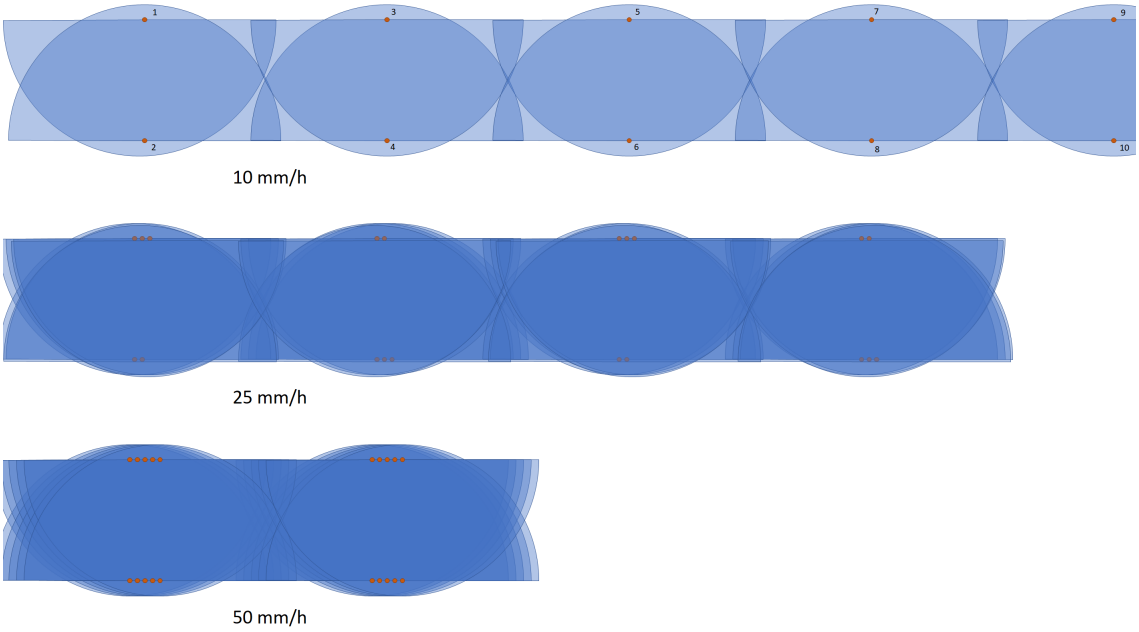

Source: Author (2023)

Assuming that one rotator sprinkler produces a rainfall with the intensity of $5\,\mathrm{mm/h}$ (discussed in Section 4.1.1), the semicircles are positioned to achieve the nominal intensity, taking into account the intersections of the circles. Areas with darker shading indicate a higher expected rainfall concentration. For instance, for the lighter rain intensity, the visual representation in the figure only captures the first ten sprinklers. The sprinklers are strategically placed facing each other to ensure uniformity for $10\,\mathrm{mm/h}$ rain. Next, the remaining set of sprinklers are placed at $16\,\mathrm{m}$ intervals, each aligned with the effective radius, extending until the end of the sprinkler line. The complete sprinkler locations for the three analyses are shown in Appendix A.

With the results of the water dispersion study, Table 3 has been generated to display three different rain intensities along with their corresponding maximum distances. This information pertains to the conditions achievable in the outdoor test environment.

Table 3 – CARISSMA outdoor testing facility rain capabilities

Rain Amount (mm/h)	**Distance (m)**
10	112
25	56
50	28

Source: Author (2023)

Therefore, the rain equipment is distributed in the test track acceleration area, considering the adequate overlap of the sprinklers in order to obtain the required rain intensity. Figure 24, illustrates the sprinklers arrangement for the rain intensity of $25\,\mathrm{mm/h}$.

Figure 24 – Sprinklers positioned in the outdoor facility for the rain of $25\,\mathrm{mm/h}$, lateral view

Source: Author (2023)

To ensure the reproducibility of the rain system, the position of the sprinklers and the measuring equipment is determined by means of Global Navigation Satellite System (GNSS) localization with correction, which provides an accuracy of up to $2\,\mathrm{cm}$. Figure 25 illustrates the layout for generating the outdoor synthetic rainfall intensity of $10\,\mathrm{mm/h}$. The triangular markers indicate the locations of the rotating sprinklers, which cover $112\,\mathrm{m}$ of the facility.

Figure 25 – Setup of the outdoor facility for the generation of the $10\,\mathrm{mm/h}$ rain intensity

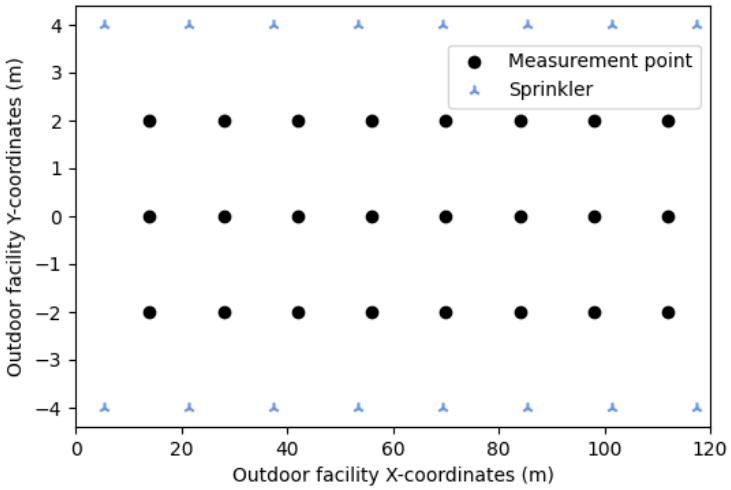

Source: Author (2023)

The circle markers indicate the designated measurement positions for the disdrometer, WeatherHat and square meter method assessment. Using 20 rotator sprinklers for the $25\,\mathrm{mm/h}$ intensity, rain is generated only in the first $56\,\mathrm{m}$ of the outdoor facility, as shown in Figure 26.

Figure 26 – Setup of the outdoor facility for the generation of the $25\,\mathrm{mm/h}$ rain intensity

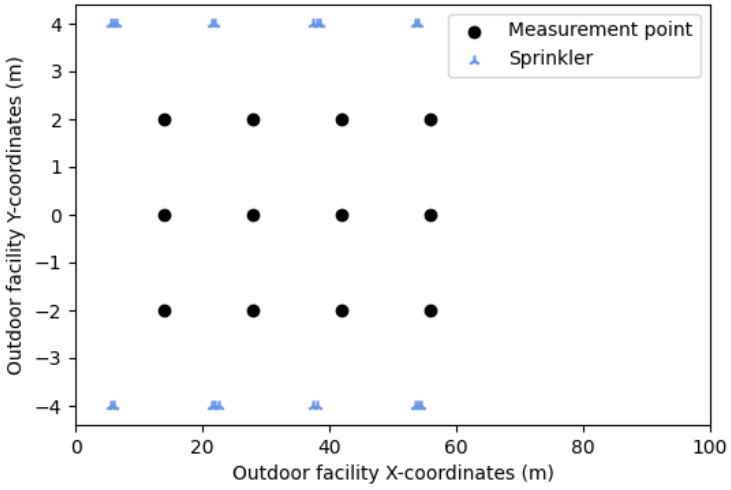

Source: Author (2023)

Lastly, in the case of rain intensity of $50\,\mathrm{mm/h}$, four groups of five rotator sprinklers are used, as illustrated in Figure 27 and the total distance is $28\,\mathrm{m}$. The sprinklers setup of the three intensities are implemented with this approach in anticipation of the upcoming project phase, where data collection is planned to occur by utilizing sensors located in the position $(0,\ 0)$ of the figures, along with strategically positioned targets within the facility.

Figure 27 – Setup of the outdoor facility for the generation of the $50\,\mathrm{mm/h}$ rain intensity

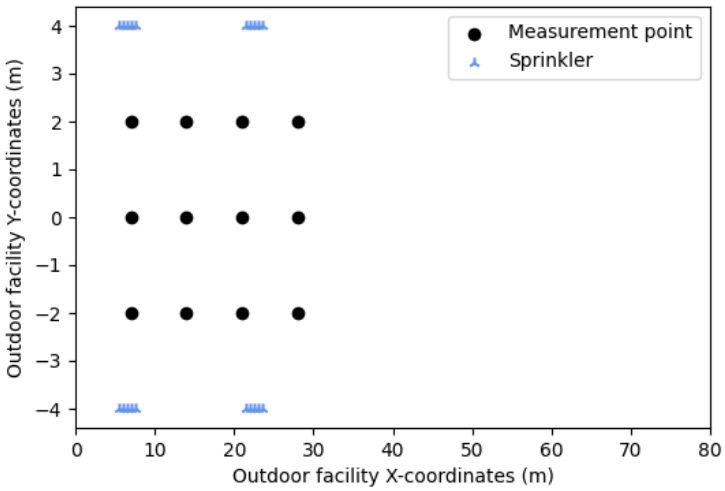

Source: Author (2023)

The DSDs curves, square meter method as well as the intensity obtained from the WeatherHat are compared in all measurement points. The records are collected over one minute at each point for the disdrometer and the WeatherHat. The data collection of the square meter method is shown in Figure 28 and is collected over 30 minutes.

Figure 28 – Data acquisition of the square meter method

Source: Author (2023)

After completing the rain data collection, the primary objective is to analyze the diverse results of the generated rain intensities. A comparative evaluation is conducted among the three distinct rain intensities. Due to variations in their generation distances along the x-axis within the facility, a standardized measurement coordinate is selected: x $= 28$ m and y $= 0$ m. This comparison specifically involves assessing the outputs from the disdrometer.

The next purpose of this analysis is to understand the uniformity of the rain over the segmented area, over the duration of the test, to assess the influence of wind in the generation of synthetic rain outdoors, and to evaluate the reliability of the measurement systems in the test facility. For this step, each rain intensity is analyzed separately. For the disdrometer measurements, the methodology is to construct the DSD graphs with two different approaches performed in the sprinkler array:

- Consistency of the rain distribution on the longitudinal range, comparing all the X positions for one specific Y position;
- Consistency of the rain distribution on the lateral range, comparing all the Y positions for one specific X position.

In this way, it is possible to understand the uniformity of the synthetic rain in both directions of the test facility. As for the outcomes of the square meter method, heatmaps are

chosen as the representation method, bringing a good visualization of the rainfall in the test facility. A comparison analysis between the findings of both instruments is performed. Finally, the results of the WeatherHat data are compared between the three rain intensities.

3.1.2.3 Outdoor Synthetic Rain Comparison

To identify possible limitations of the outdoor synthetic test, rainfall data from the well-established Cerema PAVIN Fog and Rain indoor facility in France are compared with the CARISSMA results. The indoor facility, Figure 29, is capable of producing rainfall rates from $17\,\mathrm{mm/h}$ to $175\,\mathrm{mm/h}$ (Rivera et al., 2022). This facility is selected for analysis due to its affiliation with the research project encompassing this work, thus providing accessible data for comparative purposes. Data from four rain intensities are analyzed using the square meter method, the WeatherHat and the disdrometer.

Figure 29 – Cerema PAVIN fog & rain facility

Source: (Liandrat et al., 2022)

Alternatively, the CARISSMA synthetic rain is correlated with the Marshall-Palmer DSD model, which is referenced in Section 2.7. The detailed results of these comparisons are presented in the following chapter.

3.1.2.4 Real Rain Data Versus Outdoor Synthetic Rain

To validate if the C-IAD synthetic rain has similar characteristics to real rain, the disdrometer is placed outdoors to collect continuous DSDs of the environment over a period of 5 days, producing a total amount of over 6700 minutes of recorded data. An initial data processing is required to identify the rainy periods. A code is developed in Python to calculate the number of drops detected by the disdrometer in each minute. If the number of drops exceeds 100, that minute is considered a rainy period, since there are raindrops on the data.

For these files, the DSD curves are compared to the synthetic outdoor rain data. However, the square meter method is not performed for real rain, and despite the disdrometer's ability to provide rain intensities, it is unsuitable for application to artificial rain. Therefore, to compare the different DSDs and to overcome this limitation of not having rain intensity records for real rain, the concept of water volume derived from the DSDs is introduced. This concept is based on the assumption that small raindrops assume a spherical shape, so the volume (V) is defined by

$$V = \sum_{i=1}^{n} \frac{4}{3} \pi r_i^3, \tag{4}$$

where r_i is the radium of each drop of water and the sum encompasses the different drop's diameters measured in the disdrometer. With the aim of drawing comparisons, the approach involves comparing the DSD curves that have similar drop volumes.

The Root Mean Square Error (RMSE) is used as the evaluation method. The RMSE can be conceptualized as a representation of the standard deviation that characterizes the differences between the measurements and a reference curve (Jokela et al., 2019). The equation is defined as

$$RMSE = \sqrt{\frac{\sum_{i=1}^{n} (S_i - O_i)^2}{n}}, \tag{5}$$

where S_i is the quantity of drop per diameter from the artificial rainfalls, O_i the values for the real rain drops and n the total number of diameter classes, equals to 22 as specified in section 3.1.1. Therefore, Equation 5 is used to compare the CARISSMA rain curves with the real rain DSDs.

3.2 WEATHER CONDITIONS EFFECTS ON SENSOR DATA

This section describes the sensor data acquisition tests performed at the CARISSMA outdoor facility, detailing the equipment used and the datasets recorded. It also presents the methodology used to analyze the impact of adverse weather conditions on the perception sensor data.

3.2.1 Sensor Data Acquisition

The data set is established with the purpose of studying the effects of adverse weather conditions on different sensors and is performed at the Technische Hochschule Ingolstadt - CARISSMA outdoor proving ground in Ingolstadt, Germany. The sensors used in this data recording are integrated in a single setup. Figure 30 shows the structure which includes an RGB Camera, a Thermal Camera, an Imaging Radar, a MEMS Lidar and a 360° Lidar.

Figure 30 – Sensors setup

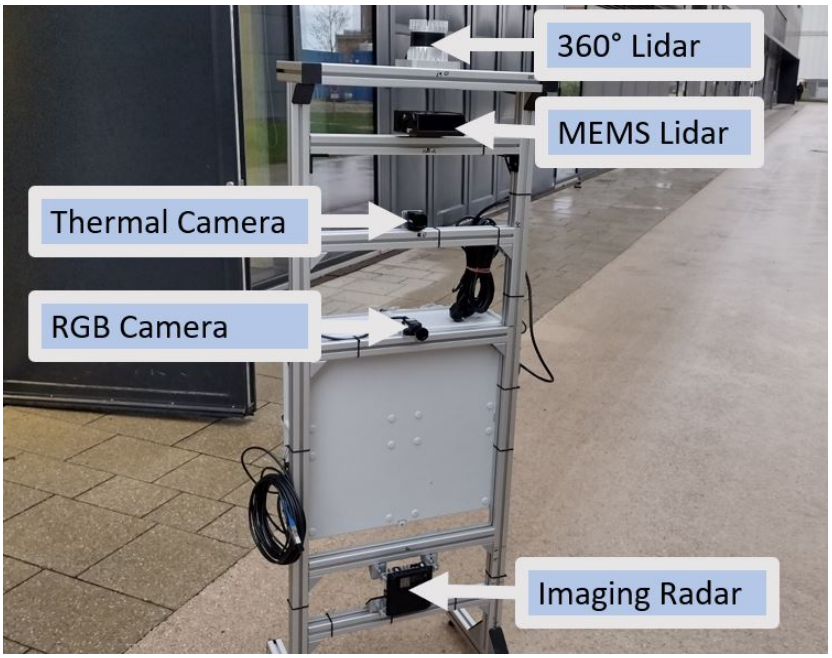

Source: Author (2023)

Measurements are conducted under a variety of conditions to fully evaluate the weather impact in the perception sensors. These include assessments in clear weather and across the three distinct rain intensities specifically generated within this dissertation. In addition, measurements are performed during both daytime and nighttime settings. The latter one is done without any artificial light in the facility. The process extends over four days of data collection and the detailed schedule is outlined in Table 4.

Table 4 – Sensor data acquisition cronogram

Day	**Shift**	**Activity**
First	Morning	Set/Measure position of all Targets/Sprinkles/Sensor setup
First	Afternoon	Conduct Test Dry Day
First	Night	Conduct Test Dry Night
Second	Morning	Mount & Validate Rain Facility 10 mm/h
Second	Afternoon	Data Collection 10mm/h Day
Second	Night	Data Collection 10mm/h Night
Thirdy	Morning	Mount & Validate Rain Facility 25 mm/h
Thirdy	Afternoon	Data Collection 25mm/h Day
Thirdy	Night	Data Collection 25mm/h Night
Fourth	Morning	Mount & Validate Rain Facility 50 mm/h
Fourth	Afternoon	Data Collection 50mm/h Day
Fourth	Night	Data Collection 50mm/h Night

Source: Author (2023)

The data collection involves the use of three distinct Euro NCAP homologated soft body targets: an adult male model, a cyclist model, and a car model, as shown in Figure 31. For the purpose of sensor noise analyses, standard targets for the three types of sensors are part of the acquisition (corner reflector for radar, calibration board for camera, and reflective surfaces for lidar). However, this dissertation does not include an examination of the data collected using these sensor noise targets.

Figure 31 – Soft body targets used in the data acquisition

Source: Author (2023)

The target position introduces two main variables. First, the distance between the target and the sensor position - $27\,\text{m}$, $55\,\text{m}$, $82\,\text{m}$, $109\,\text{m}$. Figure 32 shows each of the four positions with respect to the x-axis of the CARISSMA outdoor facility. The second variable is the orientation of the targets, which can be set as $0°$, $45°$ and $90°$ relative to the sensor orientation.

Figure 32 – Target positions for the outdoor tests with sensors

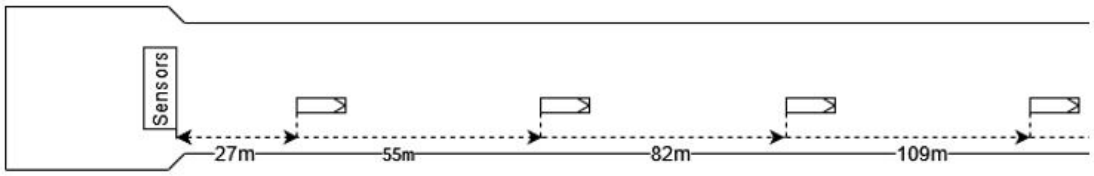

Source: Author (2023)

All three target orientations are recorded in the daytime tests. In the night tests, only the $0°$ orientation is used, being the one where the front of the target is facing away from the sensor. The four target positions in the x-axis of the outdoor facility are used for the 10 mm/h rain and clear weather tests. For the 25 mm/h tests, data collection is conducted at the first two positions and for the 50 mm/h rain, data is collected only at the 27 m position. Each test has 30 seconds of data acquisition and a comprehensive list of all the tests conducted can be found in Appendix B. In total, 176 series of sensor data are collected and, as an example, Figure 33 illustrates some records of the data acquisition.

Figure 33 – Images from the sensor data acquisition

(a) 10 mm/h (b) 25 mm/h (c) Wait period

Source: Author (2023)

Figure 33a demonstrates the data acquisition process for the car target in the $0°$ orientation during the 10 mm/h rain conditions. In Figure 33b, the bicycle target is acquired during the $0°$ orientation position and 25 mm/h rain, while Figure 33c shows the waiting period until complete darkness, marking the next phase of the test process.

In summary, the data collection is performed over four consecutive days and includes all targets in four different scenarios: daytime in clear weather, nighttime in clear weather, daytime testing with three different rain intensities, and nighttime testing with light and medium rain intensities. The 50 mm/h rain intensity was not performed at night. During the performance of these tests, natural precipitation made it impossible to collect the synthetic rain data in a controlled manner. In addition, the limited availability of the test site makes it impractical to conduct a new data collection. The next subsection explains how all this data recorded for the data set is explored.

3.2.2 Sensor Data Analysis

Of the five different sensors used to collect data, the core of the data analysis centers on the RGB camera. Section 2.5 discussed its sensitivity to rain compared to other sensors, and it was chosen for its cost-effectiveness and accessibility in the automotive field. In addition, the development of open-source camera-based algorithms is more advanced compared to the perception algorithms for radar and lidar. The analysis focuses only on the car target package, which was chosen as the target that has more sensor interaction in the real world. Table 5 highlights the selected datasets for the investigation of weather effects.

Table 5 – Data records that are analyzed

ID	Weather	Position
1	Clear	28 m
2	Clear	56 m
3	Clear	84 m
4	Clear	112 m
5	10 mm/h	28 m
6	10 mm/h	56 m
7	10 mm/h	84 m
8	10 mm/h	112 m
9	25 mm/h	28 m
10	25 mm/h	56 m
11	50 mm/h	28 m

Source: Author (2023)

The primary objective is to detect disparities in object detection based on target position parameters and to evaluate the impact of rain. Since the night tests lack the 50 mm/h rain intensity, the daylight tests are chosen for this comparative study. Also, only the positioned orientation 0° orientation is chosen because it is the more common orientation interaction between the car in the real environment. As a result, eleven cases are examined, the majority of which contain approximately 300 frames for analysis.

The analysis starts with ground truth labeling. For each case, an image is manually labeled using the GNU Image Manipulation Program (The GIMP Development Team, 2019) to identify the box coordinates (left, bottom, right, top) of the car target. This established ground truth is applied consistently to all 300 frames. Then, YOLO V7 runs to determine class information and extract the bounding boxes of the objects. The evaluation is performed using the Mean Average Precision (mAP) technique (Cartucho et al., 2018), which aims to assess the similarity between the ground truth and the detected boxes. The mAP is a numeric value between 0 and 1, calculated as the mean of the Average precision (AP). Higher mAP values indicate better accuracy and precision in detecting objects across classes. The influence of rain and target distance can be discussed by comparing the results of each test case in terms of mAP values. To compute the AP, some prior knowledge is required. First, the bounding box of the YOLO is validated against the ground truth boxes using the Intersection over Union (IoU) (Cartucho et al., 2018), defined as

$$IoU = \frac{AreaofOverlap}{AreaofUnion}. \tag{6}$$

This quantifies the degree of overlap between the predicted bounding box coordinates and the ground truth coordinates. Figure 34 showcases the difference between the two concepts of area. A high IoU value indicates that the predicted bounding box is close to the ground truth. Bounding box matching occurs when both the detected object and the ground truth object share the same label and have an IoU greater than or equal to $50\,\%$ in each frame.

Figure 34 – Difference of the areas used in the IOU calculation

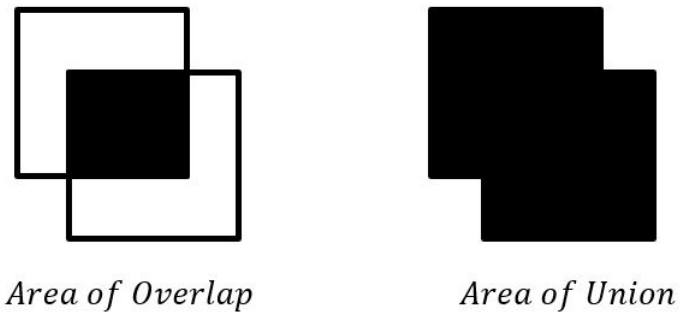

Source: Author (2023)

Confusion matrix is a tool in the field of machine learning used to assess the performance of classification algorithms and is represented in Figure 35. The matrix breaks down the outcomes into four categories: true positives (correctly identified positive cases), true negatives (correctly identified negative cases), false positives (negative cases incorrectly identified as positive), and false negatives (positive cases incorrectly identified as negative). Therefore, is a tabular representation, that summarizes the accuracy of a model's predictions by comparing them to actual ground truth values.

Figure 35 – Confusion matrix

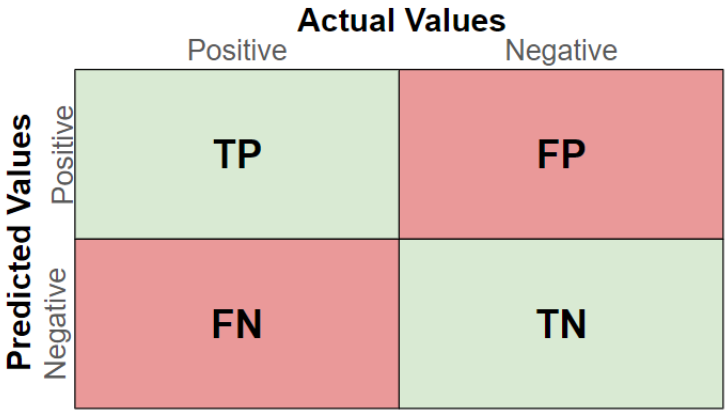

Source: Author (2023)

After the knowledge of the confusion matrix, two variables can be calculated: Precision and Recall. Precision measures the true positives, from all positive predictions, defined as

$$Precision = \frac{TP}{TP + FP}, \tag{7}$$

where TP is the number of true positives, and FP is the number of false positives. Recall quantifies the true positives of all predictions, and is described as

$$Recall = \frac{TP}{TP + FN}, \tag{8}$$

where FN is the number of false negatives. In sequence, the AP can be calculated

$$AP = \int_0^1 Precision(recall) d(recall), \tag{9}$$

where precision(recall) refers to a graphical curve that illustrates how precision and recall vary at different decision thresholds. The Average Precision (AP) is computed as the area under this precision-recall curve. By calculating the AP for each class and then taking the mean, is possible to calculate the Mean Average Precision (mAP) as

$$mAP = \frac{1}{N} \sum_{i=1}^{N} AP_1, \tag{10}$$

where AP is the average precision for a class and N is the number of classes. The mAP measures the average precision for each class and the mean average precision for all classes. Essentially, each test case contains different object classes recognized by the YOLO model. In particular, for the 'car' class, the comparison between the detection area of the boxes and the ground truth is used to compute its mAP, based on an accepted model described in the literature (Cartucho et al., 2018). Finally, this dissertation presents the potential impact of synthetic rain on perception systems, which is discussed in the following chapter.

4 RESULTS

The results chapter is divided into two sections. The first one discusses the results of the validation of the rain. It is organized into four subsections, which explain different verifications and analyses for the approval of the synthetic rain to be used in automated driving tests. The second section delves into the use of the sensor data acquisition with the study case of the interference of rain in the perception algorithms of the camera data.

4.1 SYNTHETIC RAIN RESULTS

This section presents a comprehensive overview of the results obtained from the four different approaches used to validate the outdoor synthetic rain. It begins with an analysis of the sprinklers, followed by an understanding of the outdoor synthetic rain generated. In sequence, the next subsections present the comparison between the outdoor rain with the Marshall-Palmer theoretical model, an indoor synthetic rain data and to finalize, the comparison with real rain.

4.1.1 Preliminary analysis of the sprinklers

With the volume of water collected in the experiment at the five positions on the working radius of the two types of sprinklers and applying the square meter method to calculate the rain intensities, Figure 36 is constructed. Therefore, the measured rain intensities of the rotator and the spray sprinkler can be visualized over the five evaluated positions.

Figure 36 – Rain intensity measurements for the two sprinkler types in five different positions

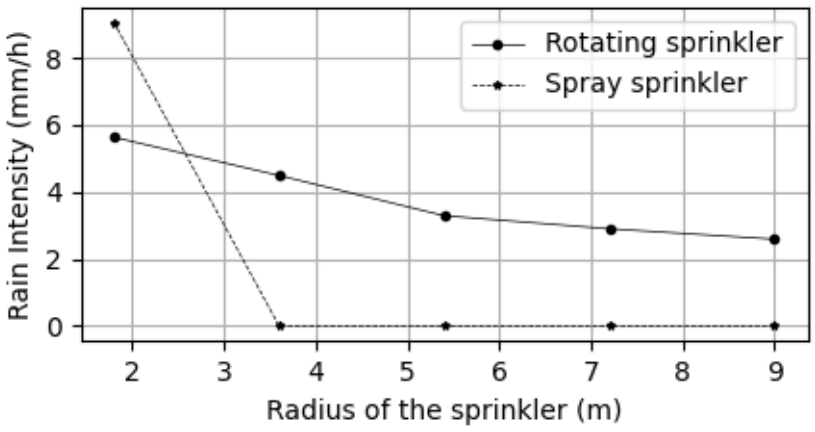

Source: Author (2023)

The spray sprinkler, represented by the dotted line in the graphic, is characterized by the higher water flow, resulting in elevated rain intensity, bigger than $8\,\mathrm{mm/h}$ at the first position. Conversely, the water deposition of the spray sprinkler presented to be limited to the $1.8\,\mathrm{m}$, as no more water is collected with the increase of the radius (zero rain intensity). In contrast, the rotating sprinkler demonstrates an uniform distribution of water drops across its effective radius, which consistently covers all measurement positions.

Therefore, the rotating sprinkler is selected as the preferred option for rain generation, even though it presents lower rain intensities compared to the spray sprinkler. To facilitate the sequential calculation of the sprinkler arrangement, the rain intensity of the rotating sprinkler, varying from 5.63 mm/h to 2.59 mm/h, is assumed to be 5 mm/h, serving as an approximate average across all five positions. In addition, the rain intensities presented to be higher in the initial positions, as can be seen in Figure 36. Assuming an average rain intensity of 5 mm/h simplifies the calculations involved in sprinkler placement. However, careful planning of sprinkler arrangement is essential to ensure that the sprinklers complement each other and provide a uniform distribution of water across the test facilities. The conclusion is that the rotator sprinklers need to be placed in pairs, with a spacing of 8 m between them. This paired placement compensates for the decreasing trend in water volume, effectively creating a uniform rain pattern.

4.1.2 Synthetic outdoor rain

This subsection tales the data collection from the disdrometer, the WeatherHat and the square meter method, as outlined in section 3.1.2.2, to analyze the synthetic outdoor rain. Beginning with the evaluation of the rain Drop Size Distribution (DSD) for all intensities measured in the facility at the common assessment position (x=28, y=0), Figure 37.

Figure 37 – The three intensities of synthetic rain DSDs measured at the outdoor facility in distance x=28 m and y=0 m

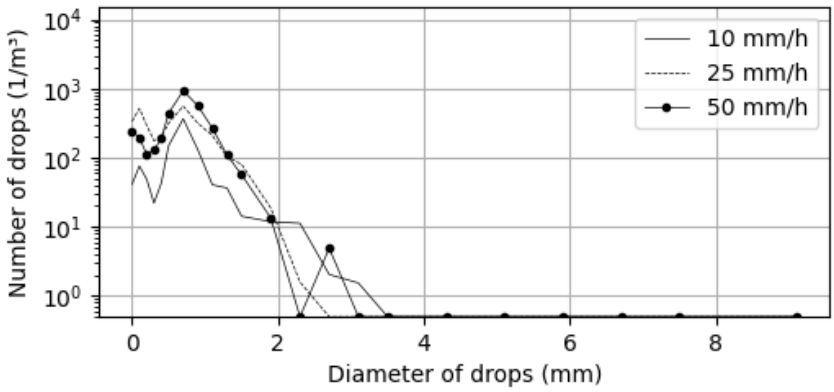

Source: Author (2023)

The figure shows that the majority of the drops in the three curves are concentrated in the diameter range of 1 mm to 2 mm. In comparison, the occurrence of larger drops is less frequent, and there are no drops larger than 4mm in any case. It is worth noting that the overall count of drops remains relatively high for diameters smaller than 2 mm, and the curves follow a similar structure. Also, the peaks are higher as the intensity increases. Thus, the solid line representing the rain intensity of 10 mm/h has a smaller area across the curve compared to the line with points, the 50 mm/h rain.

The results, represented in Figure 37, exhibit a coherent pattern, highlighted by the rain intensity curve of 25 mm/h, which converges between the other two curves. This alignment alludes to a consistency of the measurements, where higher rain intensities denote a greater absolute amount of raindrops.

The next step is to analyze each rain intensity result separately. The results from the disdrometer readings are presented, followed by the heatmaps from the square meter method and then a comparative analysis of the two is performed. Beginning with the lower rain intensity, Figure 38 provides the 10 mm/h DSDs for the longitudinal and lateral ranges. For the longitudinal evaluation, is opted to select only three specific distances (the beginning, middle and end of the test facility) in order to simplify the graph representation. This decision is based on the consideration that the inclusion of eight DSD curves for the respective measurement points results in visual disturbance within a single graphic.

Figure 38 – DSDs of synthetic rain at outdoor facility – nominal intensity of 10 mm/h, with the longitudinal and lateral analyses

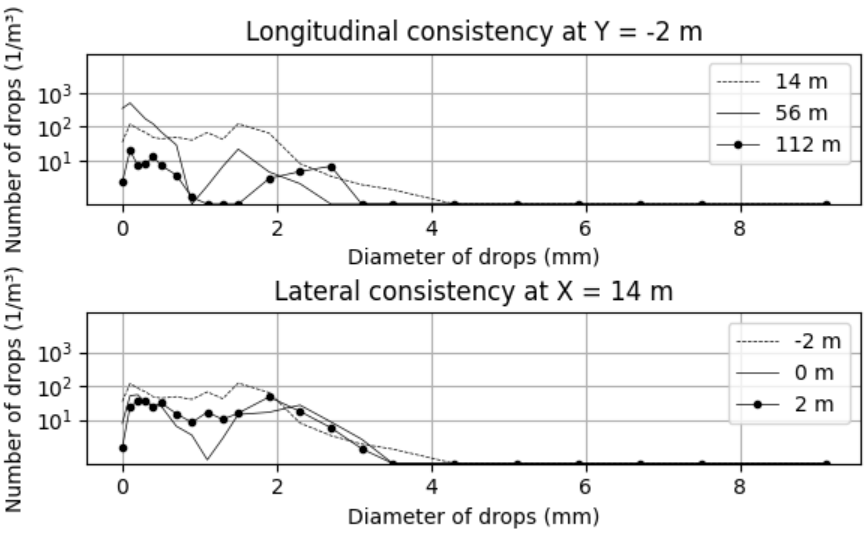

Source: Author (2023)

Figure 38 shows the longitudinal evaluation, where all diameters are concentrated up to 4 mm. The dotted line is the DSD of 14 m and has the extended area under the curve, so a more intense rainfall is evident. In contrast, the curve with dots, representing the distance of 112 m, has fewer drops in the measured DSD. The lower graph shows that for the lateral evaluation, the point on the right side of the test facility (-2 m) has higher drops registered compared to the other lateral positions. Conversely, the curves are closer in shape than those of the longitudinal results. Figure 39 presents the heatmap for the 10 mm/h rain, based on the measures with the square meter method. The darker regions represent rain intensities closer to 14 mm/h, while the lighter ones reach values of 2 mm/h. The result indicates that the uniformity remains up to 80 m, in which the intensity is between 8 mm/h and 14 mm/h. Beyond the range of 80 m, intensities decrease to rains below 8 mm/h, reaching insignificant values of intensity.

Figure 39 – Intensity heatmap of synthetic rain at outdoor facility – nominal intensity of 10 mm/h

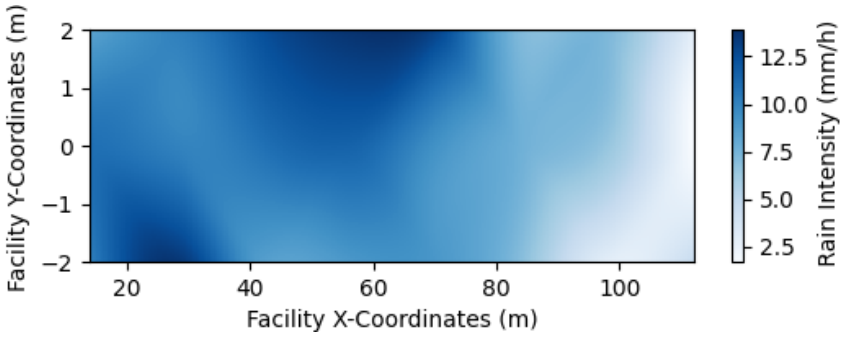

Source: Author (2023)

The highlight peaks of rainfall occur close to $(21,-2)$ and $(60,2)$ coordinates, denoted as (X,Y). A notable similarity can be discerned between Figure 38 and Figure 39, as both offer analogous findings. For instance, at 112 m, an absence of drops is evident, while at 14 m, the peaks are significant at -2 m, followed by 0 m and 2 m. These trends are apparent in both images, represented differently, but handed the same outcome. This observation supports the conclusion that the square meter method aligns with the findings of the disdrometer. The same conclusion can be extended for the other two rain intensities. Figure 40 shows the dual analysis of the disdrometer data for the 25 mm/h rain.

Figure 40 – DSDs of synthetic rain at outdoor facility – nominal intensity of 25 mm/h, with the longitudinal and lateral analyses

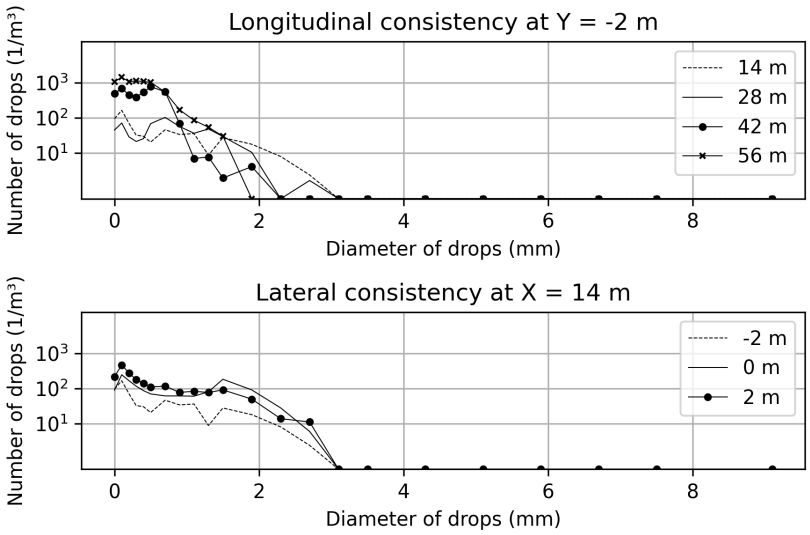

Source: Author (2023)

Since for this rain intensity only four measurement points are presented in the longitudinal position of the facility, all DSDs are plotted. It can be seen that the lines with solid markers, appear with more water in the area. The lateral results, showed similar curves, so a good uniformity. Figure 41 illustrates the results of the square method.

Figure 41 – Intensity heatmap of synthetic rain at outdoor facility – nominal intensity of 25 mm/h

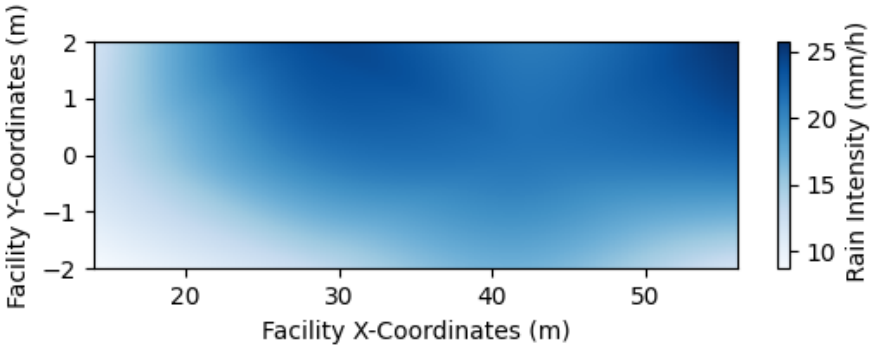

Source: Author (2023)

It is also noticeable good uniformity of the water and the rain peaks are at the distance 56 m followed by the 42 m, which can be seen in both analyses, as well as in both figures that the rain at Y $=$ -2 m has the lower rain intensity, confirming the agreement between the two approaches. Figure 42 shows the DSDs for the rain intensity of 50 mm/h.

Figure 42 – DSDs of synthetic rain at outdoor facility – nominal intensity of 50 mm/h, with the longitudinal and lateral analyses

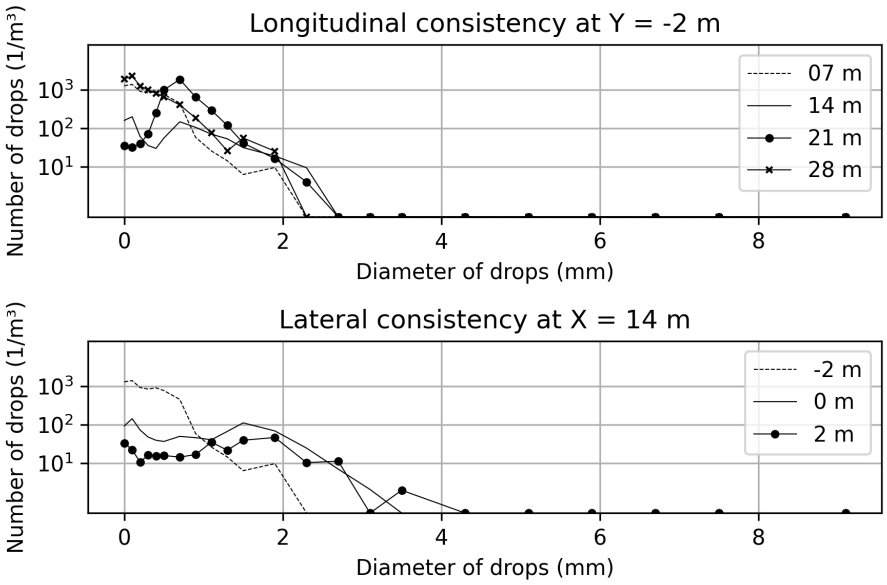

Source: Author (2023)

In the longitudinal analysis, the position equal to 28 m has the higher peaks, and for the lateral measurements, the curves have different shapes and values. The same problem can be seen in Figure 43, which shows the results of the square method for the rain intensity of 50 mm/h. There is no rain uniformity in the test facility. Therefore, the outcomes do not deliver the expected rain intensity values. There is a significant variance within the range of the heatmap, and notably, no data points register an intensity of 50 mm/h.

Figure 43 – Intensity heatmap of synthetic rain at outdoor facility – nominal intensity of 50 mm/h

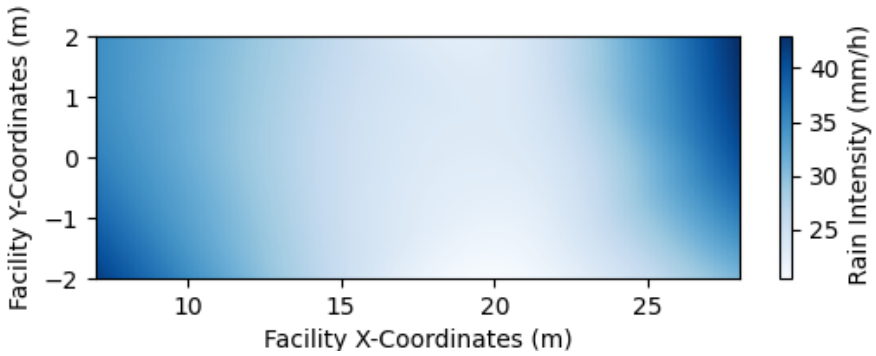

Source: Author (2023)

Even more curious is that for this nominal intensity, the longitudinal distance is the lowest among all the tests. So, there are more sprinklers per area, which should represent more water. However, the majority of recorded rain intensities are around 20 mm/h, which is less than half of the nominal value.

The heatmaps for all three intensities show a significant influence of external factors on the rain intensity measurements and the desigual values are not only limited to the expected quantification that differs by the position of the sprinklers but also reveal the influence of wind conditions during the tests, which justifies the lighter regions of the heatmaps. This phenomenon is more evident in Figure 43, where the wind conditions during this test scenario of 50 mm/h rain proved to be more challenging compared to other measurements. This observation prompts an exploration of the role of wind conditions in shaping rain uniformity. Therefore, Table 6 provides the wind data for the three rain intensities from the weather station, alongside with the rain intensity measurements average using both the square meter method and the WeatherHat.

Table 6 – Rain Intensity measurements - CARISSMA Outdoor test facility

Nominal Intensity (mm/h)	**Square meter (mm/h)**	**WeatherHat (mm/h)**	**Wind average (m/s)**
10	8.7	4.9	1.3
25	17.4	16.7	1.9
50	31.2	2709.4	45.1

Source: Author (2023)

It can be seen that the wind speed at the time of the 50 mm/h measurement test is more than 40 times higher than the other collection data, an unusually high value for the test conditions. This discrepancy explains why this particular test is the most adversely affected in terms of rain uniformity. Afterward, the average rain intensities from the square meter align with the nominal values, considering the low intensities presented in the heatmaps. As already mentioned, this phenomenon is attributed to the wind carrying the rain away from the area of

interest. Nevertheless, a disparity between the two rain measurement approaches is evident in the table. For a wind speed of $45\,\mathrm{m/s}$, the WeatherHat station is reporting $2709.4\,\mathrm{mm/h}$ of rain intensity, a non-realistic value (Thies Clima, 2022). Therefore, there is a limitation in the tipping mechanism of the WeatherHat station when in contact with higher wind speeds. It also raises the possibility of sensor interference affecting the reported wind speed value, given its exceptionally high reading. This emphasizes the critical role of accurate wind data in ensuring precise rain intensity measurements.

In summary, the sprinklers were able to deliver water for the duration of the whole test and the rain intensities of $10\,\mathrm{mm/h}$ and $25\,\mathrm{mm/h}$ presented better results of rain uniformity over the segment area. The square method proved to be a better tool for measuring rain intensities. Wind, when in higher conditions, has a notable effect on the outdoor synthetic rain generation.

4.1.3 Outdoor synthetic sain comparison

This subsection starts with the comparison between the Marshall-Palmer model and the outdoor synthetic rain. The equations of section 2.7 have been implemented for the three intensities of analysis: $10\,\mathrm{mm/h}$, $25\,\mathrm{mm/h}$ and $50\,\mathrm{mm/h}$. Figure 44 shows the results of the theoretical rain drop size distribution curves and the experimental DSDs collected by the disdrometer in the test facilities position equals to x=28 m and y=2, since is a measurement point that has data from all three intensities.

Figure 44 – Comparison between Marshall-Palmer model and the outdoor synthetic rain for the three experimental intensities

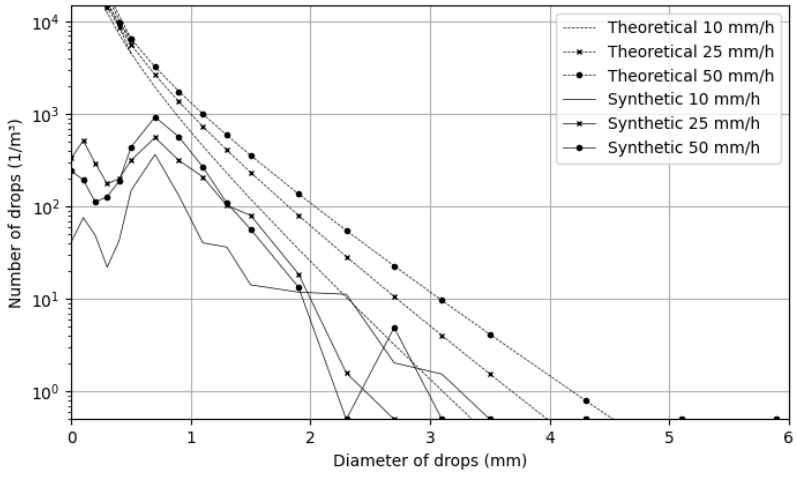

Source: Author (2023)

The theoretical results reveal a decreasing trend, illustrating that as the drop diameter increases, the number of drops decreases. Moreover, higher rain intensities correlate with a larger area under the curve, indicating a broader distribution of drop sizes. Similar trends are observed in the synthetic rain results, with decreasing curves and increasing peaks as the rain intensity rises.

The peak of the Marshall-Palmer distribution begins around 10^4, while the outdoor peaks are closer to 10^3. So, it is noteworthy that there is a requirement for an increase in the number of drops across all diameter sizes for the synthetic rain. Although the number of drops and the format of the curves differ, justified by one being experimental and the other mathematical, the observed patterns align, suggesting that the outdoor rain closely resembles the theoretical model.

Regarding the comparison between indoor and outdoor DSDs, Figure 45 shows two graphs. The upper one illustrates the comparison between the CEREMA Pavin rain of $17\,\mathrm{mm/h}$ and two corresponding CARISSMA rain intensities, since they do not have the same nominal value for comparison. The lower graphic shows the contrast between the intensities of $50\,\mathrm{mm/h}$.

Figure 45 – Comparison DSDs Indoor and Outdoor

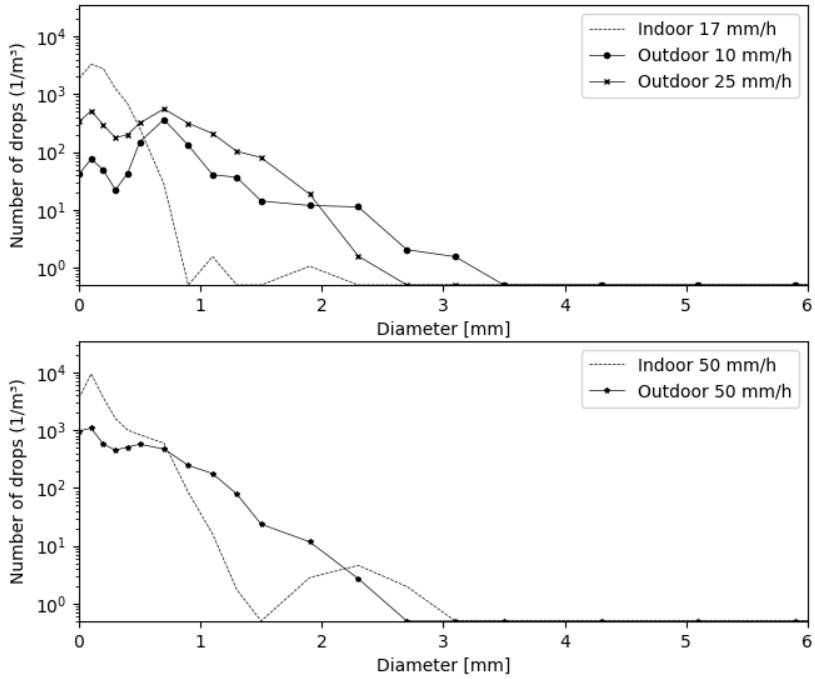

Source: Author (2023)

The indoor DSDs show an overwhelming prevalence of small drops, nearly ten times more for drops smaller than $1\,\mathrm{mm}$, coupled with a noticeable lack of larger drops. Conversely, the outdoor results demonstrate a distribution that not only differs significantly from the indoor setting but also more closely resembles the characteristics of real rain by having drops with different diameter sizes. In addition, the Cerema PAVIN Fog and Rain data are tabled to calculate the averages of the rain intensities from the square meter method and the WeatherHat. The results are presented in Table 7, excluding the wind average due to the indoor facility setting. In particular, significant deviations are observed for WeatherHat rain intensities exceeding $800\,\mathrm{mm/h}$, even in the absence of wind. The conclusion is that the limited functionality of the weather station is not only confined to wind conditions but also related to specific ranges of rain intensity.

Table 7 – Rain Intensity measurements - Cerema PAVIN Fog and Rain Indoor test facility

Nominal Intensity (mm/h)	**Square meter method (mm/h)**	**WeatherHat (mm/h)**
17	22.3	8.4
50	43.2	22.3
101	82.8	242.8
175	139.3	803.6

Source: Author (2023)

When comparing Table 6 and Table 7, it becomes evident that the values obtained through the square meter method are approximately 20% closer to the nominal intensity in indoor conditions, in other words, the results presented in the table above have a smaller gap with the set rain intensities. This observation strongly suggests that wind indeed has a significant impact on the test results.

4.1.4 Outdoor validation with real rain data

Within the 370 files capturing real rain events, the specific instances that exhibit elevated water volumes are analyzed, as shown in Figure 46, which indicates intensified rainfall during those particular minutes. The first recorded minutes and corresponding lower file index are the ones with larger volumes, so they are selected for the comparison with outdoor rain.

Figure 46 – Volume of drops in the files of real rain collected at CARISSMA.

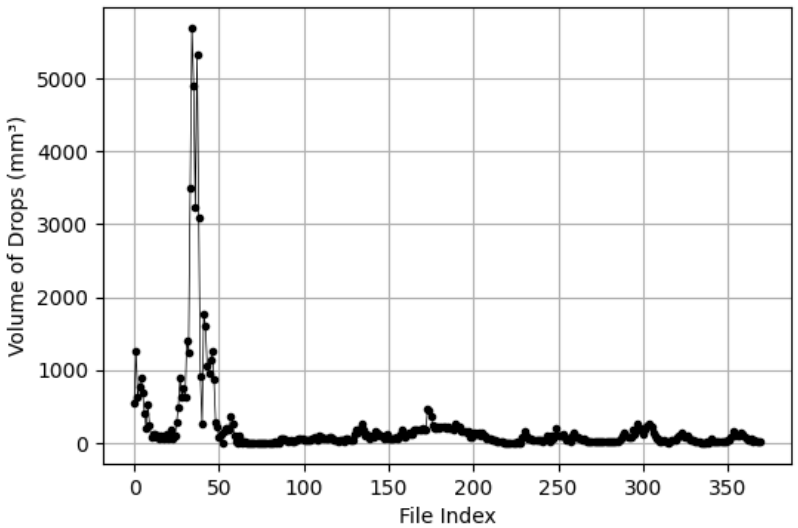

Source: Author (2023)

Due to existing doubts about the reliability of WeatherHat's rain intensity measurements, utilizing its data from real rain to compare with the synthetic one is not feasible. As a result, for

a valid comparison, the total water volume for each file of the DSD is computed. The approach involves calculating water volumes for the curves in Figure 37, and subsequently selecting real rain measurements with comparable volumes. Figure 47 shows the comparison between the real rain and CARISSMA synthetic rains, based on the volume from the DSDs.

Figure 47 – DSDs of real rain in comparison with CARISSMA synthetic data for the three rain intensities – volumetric DSD approach

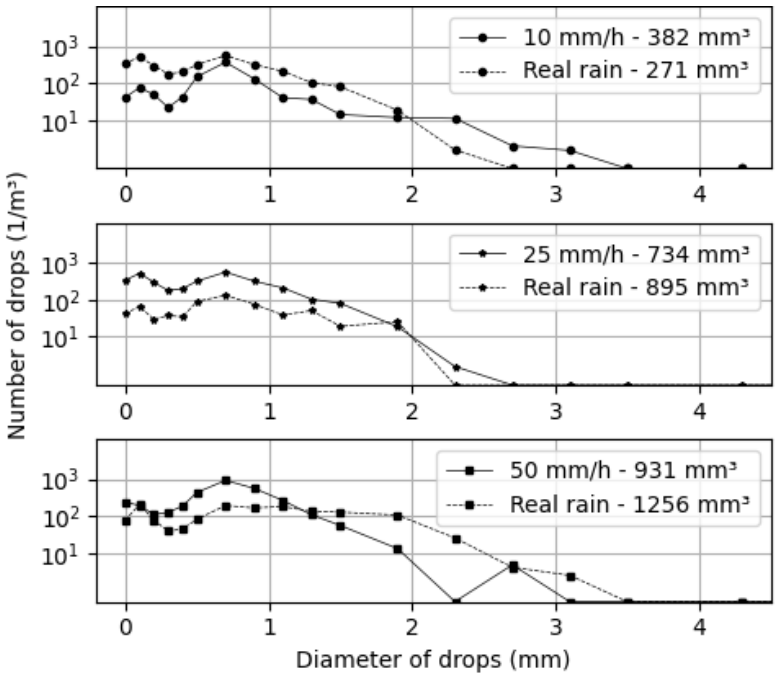

Source: Author (2023)

The comparison between the synthetic rain curves (solid lines), and the real rain data (dashed lines) provides a compelling validation of the rain generation system. For all three intensities, the curves have a similar shape, indicating that the synthetic rain closely mimics the characteristics of real rain in terms of drop size distribution. Furthermore, the observation that higher rain intensities correspond to larger volumes of water is consistent with expectations, confirming the accuracy of the rain generation system in simulating different levels of precipitation. Table 8 presents the Root Mean Square Error (RSME) results obtained by comparing the curves of real rain with those generated at the CARISSMA facility.

Table 8 – RSME of number of drops between CARISSMA rain facility and real rain

Set Rain Amount (mm/h)	**RMSE (Number of drops)**
10	53.4
25	169.1
50	202.3

Source: Author (2023)

The curve of $10\,\text{mm/h}$ exhibits the highest resemblance to real rain, reflected in the lowest RSME of $53.4\,\text{m}^3$. Importantly, the corresponding RSME values are relatively small, considering that all intensities remain in a similar order of magnitude for a number of drops, around 10^3. This underscores the effectiveness of the proposed synthetic rain generation method across the three intensity levels. The proposed synthetic rain can be improved by adding larger drops, which could be achieved by adding different sprinklers or using nets to accumulate the water and generate bigger drops, as proposed in (Hasirlioglu et al., 2016b).

4.2 SENSOR DATA RESULTS

The data of the car target captured by the RGB camera is processed, and the initial detection results are presented in Table 9. The YOLO algorithm performs a total of eleven runs, capturing class information and bounding box details for each weather condition and position.

Table 9 – Class detection from YOLO in the eleven cases

ID	Weather	Position	Detected Classes	Classes Clasification
1	Clear	28 m	2	Car; Bus
2	Clear	56 m	1	Car
3	Clear	84 m	1	Car
4	Clear	112 m	1	Car
5	10 mm/h	28 m	2	Car; Boat
6	10 mm/h	56 m	2	Car; Boat
7	10 mm/h	84 m	2	Car; Boat
8	10 mm/h	112 m	2	Car; Boat
9	25 mm/h	28 m	5	Car; Bus; Boat; Truck; Train
10	25 mm/h	56 m	2	Car; Boat
11	50 mm/h	28 m	2	Car; Boat

Source: Author (2023)

The car class consistently registers detection across all scenarios. However, in analyses involving rain, the CNN also identifies instances of the boat class. Already, can be inferred that with the presence of water in the image, the algorithm faces challenges distinguishing objects, and is trained to associate boat to water. Only in two cases, it detected other vehicles.

With the YOLO detections, the Mean Average Precision (mAP) algorithm is processed for the eleven cases and the mAP comparison is presented in Figure 48 which illustrates the results for clear weather conditions and the three intensities of synthetic rain across all target positions. In clear weather, the grid columns of the figure, YOLO achieved a detection rate of 100% for the car in all frames overall positions, which demonstrates that the distance of the target does not affect the algorithm performance. The analysis shows that the detection performance degrades in the presence of synthetic rain.

Figure 48 – Results of mAP in percentage for the eleven cases

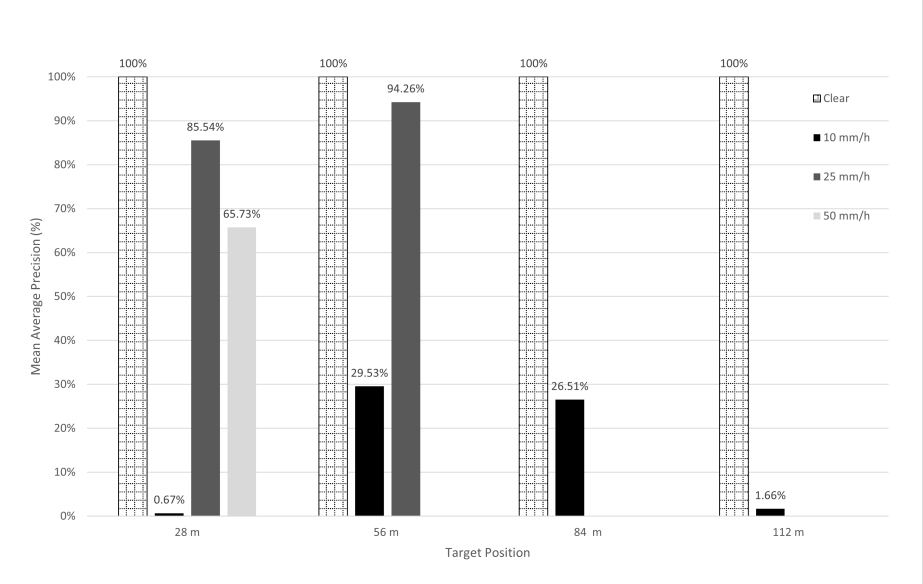

Source: Author (2023)

It was expected that the mAPs would decrease proportionally with higher rain intensities. However, the data collected in the rain of 10 mm/h is the worst among the three rain intensities, as shown by the black columns in the figure. Compared to clear weather (100% of car detection), the reduction of the mAP is between 71% and 99%. The intensity of 25 mm/h has a decrease between 5% and 15%, followed by the rain of 50 mm/h which has a decrease of more than 35% in the mAP. It is also noticed that the position does not have a correlation with the worse rain results, since the poorest result of the 10 mm/h rain is in the near target, position 28 m, with less than 1% of car detection. For an additional visualization of the results, Figure 49 shows a detection frame for all weather conditions at the target position of 28 m.

Figure 49 – Detection frames for the three rain intensities for the position target of 28 m

Source: Author (2023)

The dotted squares represent the ground truth that is labeled for each case, and the solid lines are the bounding boxes detected by YOLO. It is apparent that as the rain intensity increases, the noise in the image also escalates, which degrades the clarity of the car image. Comparing the detected bounding boxes in the image, the same results can be seen: clear weather has a perfect match between the squares, followed by the $25\,\mathrm{mm/h}$ as a closer match. It can be noticed that both rain intensities of ten and fifth have erroneous detection at the bottom of the box. It can be inferred that this arises from interference caused by the reflected water on the ground, leading to confusion in the algorithm's perception of the car's boundaries.

Moreover, the results of $10\,\mathrm{mm/h}$ and $50\,\mathrm{mm/h}$, present a brighter image, so the sun's position at the time of data collection was higher. To complete the comparison between the different cases, Figure 50 shows a radar graph of the detection results for each scenario. This includes the number of ground truth files (representing the total collected frames), the count of correctly detected cars (true positives), and instances where other vehicle classes were detected as false positives, meaning that YOLO detected objects but misclassified them.

Figure 50 – Full detection results of the YOLO perception algorithm

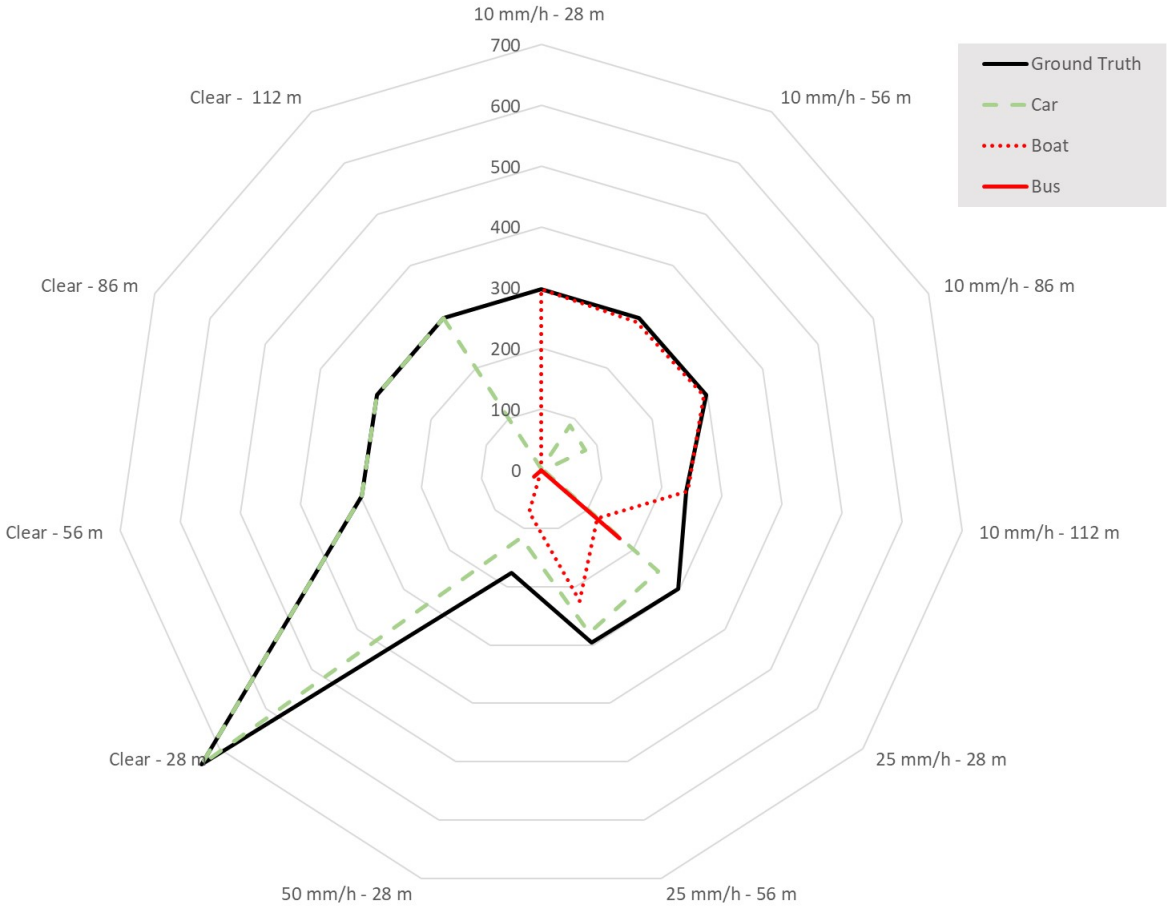

Source: Author (2023)

For almost all the cases, the analyzed frames are around 300 per test, the only one that dissociates is for the target in the closer position at the clear weather. Probability in this data acquisition the time was greater than 30 seconds. The right side and the upper part of Figure 50 shows the clear weather, it can be seen that the dotted lines for cars true positives are right above the solid lines, so it shows the 100% result of the mAP, same number of ground truths and true positive car detections. The shorter dotted line corresponds to false positives for boat detection. In the upper left part of the figure, representing the results for the 10 mm/h rain, the boat detection line is almost above the ground truth, meaning that more than 200 of false positives are detected. Conversely, the dotted line for car detections is smaller than 100, highlighting a significant issue in the data acquisition for this range of rain.

For the 25 mm/h and 50 mm/h, the car detection line is close to the ground truth line, with less space between them in the 25 mm/h. Also for this rain, it can be noticed that there are more than 150 false positives for buses (solid lighter line), which also appears as a small amount of false positives for the clear weather of position 28 m. One train and one bus were detected, but since this is an insignificant number compared to the 300 ground truth, it is not shown in the graph to better visualize the other object categories. As can be seen in Figure 50, the position of the target does not interfere with the results. To further investigate the reasons behind the low mAPs under the 10 mm/h rain, Table 10 provides a comprehensive overview of the complete outputs of the detection.

Table 10 – Outputs of mAP analysis for the synthetic rain intensity 10 mm/h

Position	mAP	Number of files	Car TP	Car FP	Boat TP	Boat FP
28 m	0.67%	297	2	0	0	297
56 m	29.53%	298	88	0	0	289
84 m	26.51%	298	79	0	0	294
112 m	1.66%	241	4	0	0	243

Source: Author (2023)

The table indicates that there are more false positive boat detections than car detections, justifying the lower values of the mAP. YOLO detects boats in the camera frames, and since the number of Car TP and Boat FP is larger than the number of frames, in some instances, there is more than one object detection per frame. Figure 51 shows one detection frame of the 10 mm/h rain and one for the 25 mm/h, both in the target position for 28 m. In the top image, YOLO incorrectly identified a boat as a false positive instead of a car as a TP, while the bottom image shows the correct class detection. It can be seen in the image that during the 10 mm/h data collection, the strong light at the time of recording significantly impacted the camera data, as corroborated by a reflection in the water on the ground, leading YOLO to interpret it as ocean instead of a road. Therefore, although there is less water in the first image, the interference from the intense light affects the algorithm's performance more.

Figure 51 – Yolo Detection Rain intensity of 10mm/h

Source: Author (2023)

In summary, the impact of rain on the performance of the perception algorithms of the camera sensors is evident throughout the analysis. The experimental results for Mean Average Precision (mAP) presented degradation under different rain intensities, showing significant challenges in object detection. In contrast, in clear weather, the algorithm exhibited good detection results when exposed to different positions, in other words, for this particular case, it detects the target from the ground truth undependable of the mark position. Thus, it is concluded that the main challenge of the algorithm under rain is not object detection, but class classification. The impact of rain, particularly at the 10,mm/h intensity, has disturbed the mAP results of the detection system. Upon closer examination of the images, it becomes apparent that the interference of strong light is also a parameter that needs to be taken into account. This interference, which is reflected in the water on the ground, introduces false positives, adding a layer of complexity to the algorithm's ability to identify object classes. These results highlight the importance of training the perception algorithms with diverse and comprehensive data sets that include different scenarios. This training equips the algorithms to effectively handle adverse weather conditions, ensuring the safe and reliable deployment of automated vehicles.

5 CONCLUSION

Proving ground testing is a critical step in the advancement of automated driving, offering controlled real conditions for rigorous evaluation. For this technology to operate reliably in adverse weather conditions, it has been discussed that synthetic weather solutions are needed, bringing many benefits such as reproducibility and control. While existing infrastructures are mainly indoor facilities, the principal contribution of this dissertation lies in proposing and validating an outdoor synthetic rain to be used in comprehensive datasets of proving ground tests in rain conditions. This advancement not only offers cost-effectiveness but also prioritizes versatility, enabling its implementation in diverse locations.

The outdoor synthetic rain developed in this work is structured to provide three distinct intensities - $10\,\mathrm{mm/h}$, $25\,\mathrm{mm/h}$ and $50\,\mathrm{mm/h}$ - demonstrated on the test facility at the CARISSMA Institute of Automated Driving. For all the intensities, an analysis of the sprinkler arrangement is conducted, which shows that it was possible to implement the three different intensities with an adequate distribution of the rain intensity over the test area. However, it is important to note the limitations of this outdoor rain generation. Due to the availability of only 20 rotator sprinklers, the medium and higher rain intensities were limited and could not be carried out within the X-coordinate capacity of the facility. Furthermore, it is evident that wind significantly impacts the measurements. Through the heatmaps, it is possible to see how the rain deviates from the measurement points, particularly noticeable during the $50\,\mathrm{mm/h}$ rain intensity. This highlights the limitations of outdoor testing when faced with high wind intensities. Consequently, there is a compelling need to integrate wind analysis into the evaluation process, allowing identification and potential exclusion of data influenced by wind.

The square meter method proves to be a more reliable approach for accurately estimating rain intensity than the WeatherHat sensor measurements. The meteorological station showed extremely high values for rain intensity in both indoor and outdoor measurements. Initially, wind was considered a potential interference with the WeatherHat's mechanical sensor that measures rain intensity, but even after conducting indoor tests that eliminate wind as a factor, it becomes clear that the WeatherHat rain sensor is inadequate to accurately measure high rain intensities, especially given the significantly inflated values recorded for the scenarios with $50\,\mathrm{mm/h}$ rain intensity. The comparative analysis of the Droplet Size Distributions (DSDs) between CARISSMA's synthetic rain and real rain data revealed a robust and positive result of the Root Mean Square Error (RMSE). The DSDs curves demonstrate a similarity in shape, especially concerning smaller diameters and peak characteristics, achieving a realistic drop distribution. Therefore, the methodology employed in this work represents a viable approach for generating outdoor artificial rain.

In terms of the sensor data acquisition, this dissertation has provided a comprehensive dataset. A consideration for the future production of outdoor datasets is to allow for a longer test interval to account for the potential occurrence of storms or high intensity of winds.

Alternatively, scheduling tests during months with historically lower rainfall may be a solution.

The analysis of the RGB camera data using neural networks and Mean Average Precision (mAP) provided insight into the performance of this perception system by analyzing the classification capabilities of the algorithm under varying weather conditions applied to the data from the camera. Observations made during clear weather conditions at different target positions showed a consistent detection pattern. This indicates that for clear weather within the distance range evaluated in this work, the algorithm is unaffected by variations in target distance. However, the transition from clear weather to rainy conditions significantly dropped detection accuracy. The mAP contrast between the two scenarios suggests that the detection algorithm's performance degrades in rainy environments.

Examination of the data revealed a particular challenge: while the algorithm successfully detects objects, it often misclassifies their object class. This problem is less indicative of the detection capability of YOLO and more representative of the algorithm's struggle to accurately determine the class of the detected objects. This finding reinforces the importance and necessity of conducting tests, such as this dissertation, to address the need for improvement - training the convolutional neural network (CNN) in the development of automated driving. By fine-tuning the algorithm through training on this dataset, there's potential to significantly improve its ability to discriminate between different object classes.

The impact of lighting conditions on the camera's performance has been previously highlighted in the literature, and the mAP analyses have demonstrated the disparity between the effects of light on camera functionality. Understanding and modulating these lighting conditions can have a crucial role in refining the accuracy of camera-based perception systems in adverse weather scenarios. Therefore, measuring the quantity of light in the test facility and the sun's position emerges as factors.

This work contributes to the academic advancement and proving ground testing of automated vehicles. To optimize outdoor testing conditions, future efforts could focus on developing strategies to mitigate wind effects in the outdoor facility. These strategies could include the implementation of structural barriers and the exploration of more advanced weather station equipment. The correlation between the DSDs of real and the outdoor synthetic rain for larger diameters shall be further explored. This could include investigating methods to introduce larger raindrops into the synthetic rain system, such as modifying nozzles, adjusting pressure, or incorporating nets. Sharing the recorded dataset with the research community remains a critical aspect of future efforts. The availability of this dataset can enable other researchers to investigate the impact of adverse weather conditions on sensor performance. Further work can also focus on refining the training approach to address misclassifications in object class detection, specifically the misclassifications of vehicles as boats due to the presence of water in the image. In addition, investigating the sun position required for effective testing and the potential use of artificial rain in machine learning applications are promising directions for future investigation.

REFERENCES

AHANGAR, M. N.; AHMED, Q. Z.; KHAN, F. A.; HAFEEZ, M. **A Survey of Autonomous Vehicles: Enabling Communication Technologies and Challenges**. v. 21. [S.l.]: MDPI AG, Jan. 2021. P. 706. DOI: 10.3390/s21030706. Available on: https://dx.doi.org/10.339www.mdpi.com/1424-8220/s21030/3/706. Cit. on pp. 24, 25.

BENMIMOUN, M.; PÜTZ, A.; ZLOCKI, A.; ECKSTEIN, L. **euroFOT: Field Operational Test and Impact Assessment of Advanced Driver Assistance Systems: Final Results**. v. 197. [S.l.: s.n.], Jan. 2013. P. 537–547. ISBN 978-3-642-33804-5. DOI: 10.1007/978-3-642-33805-2_43. Cit. on pp. 32, 34.

BROPHY, T.; MULLINS, D.; PARSI, A.; HORGAN, J.; WARD, E.; DENNY, P.; EISING, C.; DEEGAN, B.; GLAVIN, M.; JONES, E. **A Review of the Impact of Rain on Camera-Based Perception in Automated Driving Systems**. v. 11. [S.l.]: Institute of Electrical and Electronics Engineers Inc., 2023. P. 67040–67057. DOI: 10.1109/ACCESS.2023.3290143. Cit. on pp. 30, 34.

BROWN, A.; GONDER, J.; REPAC, B. **An analysis of possible energy impacts of automated vehicles**. [S.l.]: Springer, 2014. P. 137–153. Cit. on pp. 7, 19.

BRZOZOWSKI, M.; PARCZEWSKI, K. **Validating Adverse Weather Influence on LiDAR with an Outdoor Rain Simulator**. [S.l.]: Springer International Publishing, 2023. P. 12–22. DOI: 10.1007/978-3-031-25863-3_2. Available on: https://doi.org/10.1007/978-3-031-25863-3%5C%5F2. Cit. on p. 34.

BULLER, W.; XIQUE, I. J.; FARD, Z. B.; DENNIS, E.; HART, B. **Evaluating Complementary Strengths and Weaknesses of ADAS Sensors**. [S.l.: s.n.], 2018. Available on: https://www.researchgate.net/publication/328968313. Cit. on p. 27.

CAMPBELL, S.; O' MAHONY, N.; KRPALKOVA, L.; RIORDAN, D.; WALSH, J.; MURPHY, A.; RYAN, C. **Sensor Technology in Autonomous Vehicles : A review**. [S.l.: s.n.], June 2018. P. 1–4. DOI: 10.1109/ISSC.2018.8585340. Cit. on pp. 26, 27.

CARTUCHO, J.; VENTURA, R.; VELOSO, M. **Robust Object Recognition Through Symbiotic Deep Learning In Mobile Robots**. [S.l.: s.n.], 2018. P. 2336–2341. Cit. on pp. 8, 52, 53.

CORDIS EU RESEARCH RESULTS. **Automated Driving Applications and Technologies for Intelligent Vehicles**. 2017. Available on: https://cordis.europa.eu/project/id/610428. Cit. on p. 19.

CUI, G.; ZHANG, W.; XIAO, Y.; YAO, L.; FANG, Z. **Cooperative Perception Technology of Autonomous Driving in the Internet of Vehicles Environment: A Review**. v. 22. [S.l.: s.n.], 2022. DOI: 10.3390/s22155535. Available on: https://www.mdpi.com/1424-8220/22/15/5535. Cit. on pp. 7, 19.

DU, J. **Understanding of Object Detection Based on CNN Family and YOLO**. v. 1004. [S.l.]: Institute of Physics Publishing, Apr. 2018. DOI: 10.1088/1742-6596/1004/1/012029. Cit. on p. 30.

EUROPEAN COMMISSION. **EU road safety policy framework 2021-2030 - next steps towards "vision zero"**. 2019. Available on: https://www.europarl.europa.eu/doceo/document/TA-9-2021-0407%5C%5FEN.html. Cit. on pp. 7, 19.

EUROPIAN PARLIAMENT. **Self-driving cars in the EU: from science fiction to reality**. 2019. Available on: https://www.europarl.europa.eu/news/en/headlines/economy/20190110STO23102/self-driving-cars-in-the-eu-from-science-fiction-to-reality. Cit. on p. 22.

FOLSOM, T. C. **Energy and autonomous urban land vehicles**. v. 31. [S.l.]: IEEE, 2012. P. 28–38. Cit. on pp. 7, 19.

FRISONI, R.; DALL'OGLIO, A.; NELSON, C.; LONG, J.; VOLLATH, C.; RANGHETTI, D.; MCMINIMY, S. **Research for tran committee–self-piloted cars: The future of road transport?** [S.l.]: EPRS: European Parliamentary Research Service, 2016. Cit. on p. 19.

GARG, K.; NAYAR, S. K. **Vision and rain**. v. 75. [S.l.: s.n.], Oct. 2007. P. 3–27. DOI: 10.1007/s11263-006-0028-6. Cit. on pp. 34–36.

GERMAN ASSOCIATION OF THE AUTOMOTIVE INDUSTRY. **Topics and Figures on the Development of the German Automotive Industry**. 2022. Available on: https://www.vda.de/dam/jcr:d5d5c2be-a0a8-4d76-9d22-1758209f04cc/VDA%5C%5F5733%5C%5FJB%5C%5F2022%5C%5FEN%5C%5FWEB%5C%5FRZ.pdf?mode=view. Cit. on p. 19.

GINI, F. **Grand Challenges in Radar Signal Processing**. v. 1. [S.l.]: Frontiers Media SA, Mar. 2021. DOI: 10.3389/frsip.2021.664232. Cit. on p. 27.

GIRSHICK, R. **Fast R-CNN**. [S.l.: s.n.], 2015. P. 1440–1448. DOI: 10.1109/ICCV.2015.169. Cit. on p. 30.

GREENBLATT, J. B.; SHAHEEN, S. **Automated vehicles, on-demand mobility, and environmental impacts**. v. 2. [S.l.]: Springer, 2015. P. 74–81. Cit. on p. 22.

HASIRLIOGLU, S. **A Novel Method for Simulation-based Testing and Validation of Automotive Surround Sensors under Adverse Weather Conditions/submitted by Sinan Hasirlioglu**. 2020. PhD thesis – Universität Linz. Cit. on pp. 20, 29, 35, 36.

HASIRLIOGLU, S.; DORIC, I.; LAUERER, C.; BRANDMEIER, T. **Modeling and simulation of rain for the test of automotive sensor systems**. [S.l.: s.n.], 2016. P. 286–291. DOI: 10.1109/IVS.2016.7535399. Cit. on p. 20.

HASIRLIOGLU, S.; KAMANN, A.; DORIC, I.; BRANDMEIER, T. **Test Methodology for Rain Influence on Automotive Surround Sensors**. [S.l.: s.n.], 2016. ISBN 9781509018895. DOI: 10.0/Linux-x86_64. Cit. on p. 64.

HUANG, W.; WANG, K.; LV, Y.; ZHU, F. **Autonomous vehicles testing methods review**. [S.l.: s.n.], 2016. P. 163–168. DOI: 10.1109/ITSC.2016.7795548. Cit. on p. 32.

HUNTER INDUSTRIES. **Hunter Industries Nozzles**. 2023. Available on: https://www.hunterindustries.com/products/nozzles. Cit. on p. 40.

JOKELA, M.; KUTILA, M.; PYYKÖNEN, P. **Testing and validation of automotive point-cloud sensors in adverse weather conditions**. v. 9. [S.l.]: MDPI AG, June 2019. DOI: 10.3390/app9112341. Cit. on pp. 20, 47.

KRIZHEVSKY, A.; SUTSKEVER, I.; HINTON, G. E. **ImageNet Classification with Deep Convolutional Neural Networks**. [S.l.: s.n.], 2012. Available on: http://code.google.com/p/cuda-convnet/. Cit. on p. 29.

KUTILA, M.; PYYKÖNEN, P.; HOLZHÜTER, H.; COLOMB, M.; DUTHON, P. **Automotive LiDAR performance verification in fog and rain**. [S.l.: s.n.], 2018. P. 1695–1701. DOI: 10.1109/ITSC.2018.8569624. Cit. on p. 30.

LAWS, J. O.; PARSONS, D. A. **The relation of raindrop-size to intensity**. v. 24. [S.l.]: Wiley Online Library, 1943. P. 452–460. Cit. on p. 35.

LI, Y.; DUTHON, P.; COLOMB, M.; IBANEZ-GUZMAN, J. **What Happens for a ToF LiDAR in Fog?** v. 22. [S.l.: s.n.], 2021. P. 6670–6681. DOI: 10.1109/TITS.2020.2998077. Cit. on p. 20.

LI, Y.; IBANEZ-GUZMAN, J. **Lidar for Autonomous Driving: The Principles, Challenges, and Trends for Automotive Lidar and Perception Systems**. v. 37. [S.l.]: Institute of Electrical and Electronics Engineers Inc., July 2020. P. 50–61. DOI: 10.1109/MSP.2020.2973615. Cit. on p. 27.

LIANDRAT, S.; DUTHON, P.; BERNARDIN, F.; DAOUED, B.; BICARD, J.-L.; BICARD, J.-L. A.; LIANDRAT1, S.; DUTHON1, P.; BERNARDIN1, F.; BEN-DAOUED1, A.; BICARD1, J.-L. **A review of Cerema PAVIN fog & rain platform: from past and back to the future**. [S.l.: s.n.], 2022. Available on: https://hal.science/hal-03844483. Cit. on p. 46.

LUCID VISION LABS. **LUCID Machine Vision Cameras**. 2023. Available on: https://thinklucid.com/lucid-machine-vision-cameras/. Cit. on p. 29.

MARSHALL, J. S.; PALMER, W. M. K. **The distribution of raindrops with size**. v. 5. [S.l.: s.n.], 1948. P. 165–166. Cit. on pp. 8, 35.

MEYER, L. D. **Rainfall simulators for soil erosion research. In: Soil erosion research methods**. [S.l.]: Routledge, 2017. P. 83–104. Cit. on pp. 20, 35.

MORROW, W. R.; GREENBLATT, J. B.; STURGES, A.; SAXENA, S.; GOPAL, A.; MILLSTEIN, D.; SHAH, N.; GILMORE, E. A. **Key factors influencing autonomous vehicles' energy and environmental outcome**. [S.l.]: Springer, 2014. P. 127–135. Cit. on pp. 7, 19.

ONDRUŠ, J.; KOLLA, E.; VERTAĽ, P.; ŠARIĆ, Ž. **How Do Autonomous Cars Work?** v. 44. [S.l.: s.n.], 2020. P. 226–233. LOGI 2019 - Horizons of Autonomous Mobility in Europe. DOI: https://doi.org/10.1016/j.trpro.2020.02.049. Available on: https://www.sciencedirect.com/science/article/pii/S2352146520300995. Cit. on p. 22.

ORBBEC. **Intelligent computing for everyone everywhere.** 2020. Available on: https://orbbec3d.com/. Cit. on p. 29.

OUSTER. **OS1 lidar sensor**. 2023. Available on: https://ouster.com/products/hardware/os1-lidar-sensor. Cit. on p. 28.

PILLATH, S. **Automated vehicles in the EU**. [S.l.]: EPRS: European Parliamentary Research Service, 2016. Cit. on p. 22.

RAWAT, P. **Environment Perception for Autonomous Driving: A 1/10 Scale Implementation Of Low Level Sensor Fusion Using Occupancy Grid Mapping**. [S.l.: s.n.], 2019. Cit. on p. 26.

RIVERA, J.; KHOUDOUR, L.; SAINT PIERRE, G.; DUTHON, P.; LIANDRAT, S.; BERNARDIN, F.; FISS, S.; IVANOV, I.; PELEG, R. **Analysis of Thermal Imaging Performance under Extreme Foggy Conditions: Applications to Autonomous Driving**. v. 8. [S.l.: s.n.], Nov. 2022. P. 306. DOI: 10.3390/jimaging8110306. Cit. on p. 46.

ROSIQUE, F.; NAVARRO, P. J.; FERNÁNDEZ, C.; PADILLA, A. **A systematic review of perception system and simulators for autonomous vehicles research**. v. 19. [S.l.]: mdpi, 2019. P. 648. Cit. on pp. 26, 27.

SARAF, N. M.; HAMID, J. R. A.; KAMARUDDIN, M. H. **Specular and diffuse object extraction from a LiDAR derived Digital Surface Model (DSM)**. v. 18. [S.l.: s.n.], Feb. 2014. 012050, p. 012050. (IOP Conference Series: Earth and Environmental Science). DOI: 10.1088/1755-1315/18/1/012050. Cit. on p. 28.

SCHLAGER, B.; MUCKENHUBER, S.; SCHMIDT, S.; HOLZER, H.; ROTT, R.; MAIER, F. M.; SAAD, K.; KIRCHENGAST, M.; STETTINGER, G.; WATZENIG, D.; RUEBSAM, J. **State-of-the-Art Sensor Models for Virtual Testing of Advanced Driver Assistance Systems/Autonomous Driving Functions**. v. 3. [S.l.]: SAE International, Oct. 2020. P. 233–261. DOI: 10.4271/12-03-03-0018. Cit. on p. 29.

SEZGIN, F.; VRIESMAN, D.; STEINHAUSER, D.; LUGNER, R.; BRANDMEIER, T. **Safe Autonomous Driving in Adverse Weather: Sensor Evaluation and Performance Monitoring**. [S.l.: s.n.], 2023. P. 1–6. DOI: 10.1109/IV55152.2023.10186596. Cit. on pp. 7, 19, 33.

SKOLNIK, M. **Radar Handbook**. [S.l.]: 3rd ed. New York, 2008. Cit. on p. 27.

SOCIETY OF AUTOMOTIVE ENGINEERS. **Taxonomy and definitions for terms related to driving automation systems for on-road motor vehicles**. [S.l.]: SAE International, 2021. Cit. on p. 23.

STELLET, J.; ZOFKA, M.; SCHUMACHER, J.; SCHAMM, T.; NIEWELS, F.; ZÖLLNER, J. **Testing of Advanced Driver Assistance Towards Automated Driving: A Survey and Taxonomy on Existing Approaches and Open Questions**. [S.l.: s.n.], Sept. 2015. DOI: 10.1109/ITSC.2015.236. Cit. on p. 19.

SYNOTRONICS. **What is a tipping bucket rain gauge, and how does it work?** 2020. Available on: https://www.instrumentchoice.com.au/news/what-is-a-tipping-bucket-rain-gauge-and-how-does-it-work. Cit. on p. 39.

THE GIMP DEVELOPMENT TEAM. **GIMP**. [S.l.: s.n.], 12 June 2019. Available on: https://www.gimp.org. Cit. on p. 52.

THIES CLIMA. **3D Stereo disdrometer: datasheet.** [S.l.], 2022. Cit. on pp. 38, 39, 60.

TITU, A. M.; STANCIU, A.; MIHAESCU, L. **Technological and ethical aspects of autonomous driving in a multicultural society**. [S.l.: s.n.], 2020. P. 1–6. Cit. on p. 25.

UIJLENHOET, R.; SEMPERE TORRES, D. **Measurement and parameterization of rainfall microstructure**. v. 328. [S.l.: s.n.], 2006. P. 1–7. Measurement and Parameterization of Rainfall Microstructure. DOI: https://doi.org/10.1016/j.jhydrol.2005.11.038. Available on: https://www.sciencedirect.com/science/article/pii/S0022169405006311. Cit. on p. 35.

VELASCO-HERNANDEZ, G.; YEONG, D. J.; BARRY, J.; WALSH, J. **Autonomous Driving Architectures, Perception and Data Fusion: A Review**. [S.l.: s.n.], Sept. 2020. DOI: 10.1109/ICCP51029.2020.9266268. Cit. on p. 26.

VRIESMAN, D.; THÖRESZ, B.; STEINHAUSER, D.; ZIMMER, A.; BRITTO, A.; BRANDMEIER, T. **An Experimental Analysis of Rain Interference on Detection and Ranging Sensors**. [S.l.]: Institute of Electrical and Electronics Engineers Inc., Sept. 2020. ISBN 9781728141497. DOI: 10.1109/ITSC45102.2020.9294505. Cit. on p. 31.

WANG, C.-Y.; BOCHKOVSKIY, A.; LIAO, H.-Y. M. **YOLOv7: Trainable bag-of-freebies sets new state-of-the-art for real-time object detectors**. [S.l.: s.n.], 2022. Cit. on p. 30.

WANG, Z.; WU, Y.; NIU, Q. **Multi-Sensor Fusion in Automated Driving: A Survey**. v. 8. [S.l.]: Institute of Electrical and Electronics Engineers Inc., 2020. P. 2847–2868. DOI: 10.1109/ACCESS.2019.2962554. Cit. on p. 29.

YEONG, D. J.; VELASCO-HERNANDEZ, G.; BARRY, J.; WALSH, J. **Sensor and Sensor Fusion Technology in Autonomous Vehicles: A Review**. v. 21. [S.l.: s.n.], 2021. DOI: 10.3390/s21062140. Available on: https://www.mdpi.com/1424-8220/21/6/2140. Cit. on pp. 26, 28.

ZANG, S.; DING, M.; SMITH, D.; TYLER, P.; RAKOTOARIVELO, T.; KAAFAR, M. A. **The Impact of Adverse Weather Conditions on Autonomous Vehicles: How Rain, Snow, Fog, and Hail Affect the Performance of a Self-Driving Car**. v. 14. [S.l.: s.n.], 2019. P. 103–111. DOI: 10.1109/MVT.2019.2892497. Cit. on p. 30.

ZF PRESS. **Automated Driving Functions: ZF Captures Contract for 4D Full-Range Radar with Chinese OEM**. 2021. Available on: https://press.zf.com/press/en/releases/release%5C%5F25856.html. Cit. on p. 26.

ZHANG, Y.; CARBALLO, A.; YANG, H.; TAKEDA, K. **Perception and sensing for autonomous vehicles under adverse weather conditions: A survey**. v. 196. [S.l.]: Elsevier B.V., Feb. 2023. P. 146–177. DOI: 10.1016/j.isprsjprs.2022.12.021. Cit. on pp. 30, 31, 33.

ZONG, W.; ZHANG, C.; WANG, Z.; ZHU, J.; CHEN, Q. **Architecture Design and Implementation of an Autonomous Vehicle**. v. 6. [S.l.: s.n.], 2018. P. 21956–21970. Available on: https://api.semanticscholar.org/CorpusID:13719357. Cit. on p. 24.

Appendix

APPENDIX A – SPRINKLERS POSITION AT CARISSMA TEST

Rain Intensity	**10 mm/h**		**25 mm/h**		**50 mm/h**	
Sprinkler	Position x	Position y	Position x	Position y	Position x	Position y
Sprinkler 1	5.5	4	5.5	4	5.5	4
Sprinkler 2	5.5	-4	5.5	-4	5.5	-4
Sprinkler 3	21.5	4	21.5	4	6	4
Sprinkler 4	21.5	-4	21.5	-4	6	-4
Sprinkler 5	37.5	4	37.5	4	6.5	4
Sprinkler 6	37.5	-4	37.5	-4	6.5	-4
Sprinkler 7	53.5	4	53.5	4	7	4
Sprinkler 8	53.5	-4	53.5	-4	7	-4
Sprinkler 9	69.5	4	6	4	7.5	4
Sprinkler 10	69.5	-4	6	-4	7.5	-4
Sprinkler 11	85.5	4	22	4	21.5	4
Sprinkler 12	85.5	-4	22	-4	21.5	-4
Sprinkler 13	101.5	4	38	4	22	4
Sprinkler 14	101.5	-4	38	-4	22	-4
Sprinkler 15	117.5	4	54	4	22.5	4
Sprinkler 16	117.5	-4	54	-4	22.5	-4
Sprinkler 17	-	-	6.5	4	23	-4
Sprinkler 18	-	-	22.5	-4	23	-4
Sprinkler 19	-	-	38.5	4	23.5	-4
Sprinkler 20	-	-	54.5	-4	23.5	-4

APPENDIX B – CARISSMA TEST SENSOR DATA ACQUISITION

Test	Description	Sprinkler position	Target	Distance (m)	Angle
1.1	Dry - Day	Position 1	Pedestrian	28	0°
1.2	Dry - Day	Position 1	Pedestrian	28	45°
1.3	Dry - Day	Position 1	Pedestrian	28	90°
1.4	Dry - Day	Position 1	Pedestrian	56	0°
1.5	Dry - Day	Position 1	Pedestrian	56	45°
1.6	Dry - Day	Position 1	Pedestrian	56	90°
1.7	Dry - Day	Position 1	Pedestrian	84	0°
1.8	Dry - Day	Position 1	Pedestrian	84	45°
1.9	Dry - Day	Position 1	Pedestrian	84	90°
1.10	Dry - Day	Position 1	Pedestrian	112	0°
1.11	Dry - Day	Position 1	Pedestrian	112	45°
1.12	Dry - Day	Position 1	Pedestrian	112	90°
1.13	Dry - Day	Position 1	Bicycle	28	0°
1.14	Dry - Day	Position 1	Bicycle	28	45°
1.15	Dry - Day	Position 1	Bicycle	28	90°
1.16	Dry - Day	Position 1	Bicycle	56	0°
1.17	Dry - Day	Position 1	Bicycle	56	45°
1.18	Dry - Day	Position 1	Bicycle	56	90°
1.19	Dry - Day	Position 1	Bicycle	84	0°
1.20	Dry - Day	Position 1	Bicycle	84	45°
1.21	Dry - Day	Position 1	Bicycle	84	90°
1.22	Dry - Day	Position 1	Bicycle	112	0°
1.23	Dry - Day	Position 1	Bicycle	112	45°
1.24	Dry - Day	Position 1	Bicycle	112	90°
1.25	Dry - Day	Position 1	Car	28	0°
1.26	Dry - Day	Position 1	Car	28	45°
1.27	Dry - Day	Position 1	Car	28	90°
1.28	Dry - Day	Position 1	Car	56	0°
1.29	Dry - Day	Position 1	Car	56	45°
1.30	Dry - Day	Position 1	Car	56	90°
1.31	Dry - Day	Position 1	Car	84	0°
1.32	Dry - Day	Position 1	Car	84	45°
1.33	Dry - Day	Position 1	Car	84	90°
1.34	Dry - Day	Position 1	Car	112	0°
1.35	Dry - Day	Position 1	Car	112	45°
1.36	Dry - Day	Position 1	Car	112	90°

Test	Description	Sprinkler position	Target	Distance (m)	Angle
1.37	Dry - Day	Position 1	Corner reflector	112	0°
1.38	Dry - Day	Position 1	Corner reflector	56	0°
1.39	Dry - Day	Position 1	Corner reflector	84	0°
1.4	Dry - Day	Position 1	Corner reflector	112	0°
1.41	Dry - Day	Position 1	LiDAR targets	28	0°
1.42	Dry - Day	Position 1	LiDAR targets	56	0°
1.43	Dry - Day	Position 1	LiDAR targets	84	0°
1.44	Dry - Day	Position 1	LiDAR targets	112	0°
1.41	Dry - Day	Position 1	Camera targets	28	0°
1.42	Dry - Day	Position 1	Camera targets	56	0°
1.43	Dry - Day	Position 1	Camera targets	84	0°
1.44	Dry - Day	Position 1	Camera targets	112	0°
2.1	Dry - Night	Position 1	Pedestrian	28	0°
2.2	Dry - Night	Position 1	Pedestrian	56	0°
2.3	Dry - Night	Position 1	Pedestrian	84	0°
2.4	Dry - Night	Position 1	Pedestrian	112	0°
2.5	Dry - Night	Position 1	Bicycle	28	0°
2.6	Dry - Night	Position 1	Bicycle	56	0°
2.7	Dry - Night	Position 1	Bicycle	84	0°
2.8	Dry - Night	Position 1	Bicycle	112	0°
2.9	Dry - Night	Position 1	Car	28	0°
2.10	Dry - Night	Position 1	Car	56	0°
2.11	Dry - Night	Position 1	Car	84	0°
2.12	Dry - Night	Position 1	Car	112	0°
2.13	Dry - Night	Position 1	Corner reflector	28	0°
2.14	Dry - Night	Position 1	Corner reflector	56	0°
2.15	Dry - Night	Position 1	Corner reflector	84	0°
2.16	Dry - Night	Position 1	Corner reflector	112	0°
2.17	Dry - Night	Position 1	LiDAR targets	28	0°
2.18	Dry - Night	Position 1	LiDAR targets	56	0°
2.19	Dry - Night	Position 1	LiDAR targets	84	0°
2.20	Dry - Night	Position 1	LiDAR targets	112	0°
2.21	Dry - Night	Position 1	Camera targets	28	0°
2.22	Dry - Night	Position 1	Camera targets	56	0°
2.23	Dry - Night	Position 1	Camera targets	84	0°
2.24	Dry - Night	Position 1	Camera targets	112	0°
3.1	10 mm/h - Day	Position 1	Pedestrian	28	0°
3.2	10 mm/h - Day	Position 1	Pedestrian	28	45°

Test	Description	Sprinkler position	Target	Distance (m)	Angle
3.3	10 mm/h - Day	Position 1	Pedestrian	28	90°
3.4	10 mm/h - Day	Position 1	Pedestrian	56	0°
3.5	10 mm/h - Day	Position 1	Pedestrian	56	45°
3.6	10 mm/h - Day	Position 1	Pedestrian	56	90°
3.7	10 mm/h - Day	Position 1	Pedestrian	84	0°
3.8	10 mm/h - Day	Position 1	Pedestrian	84	45°
3.9	10 mm/h - Day	Position 1	Pedestrian	84	90°
3.10	10 mm/h - Day	Position 1	Pedestrian	112	0°
3.11	10 mm/h - Day	Position 1	Pedestrian	112	45°
3.12	10 mm/h - Day	Position 1	Pedestrian	112	90°
3.13	10 mm/h - Day	Position 1	Bicycle	28	0°
3.14	10 mm/h - Day	Position 1	Bicycle	28	45°
3.15	10 mm/h - Day	Position 1	Bicycle	28	90°
3.16	10 mm/h - Day	Position 1	Bicycle	56	0°
3.17	10 mm/h - Day	Position 1	Bicycle	56	45°
3.18	10 mm/h - Day	Position 1	Bicycle	56	90°
3.19	10 mm/h - Day	Position 1	Bicycle	84	0°
3.20	10 mm/h - Day	Position 1	Bicycle	84	45°
3.21	10 mm/h - Day	Position 1	Bicycle	84	90°
3.22	10 mm/h - Day	Position 1	Bicycle	112	0°
3.23	10 mm/h - Day	Position 1	Bicycle	112	45°
3.24	10 mm/h - Day	Position 1	Bicycle	112	90°
3.25	10 mm/h - Day	Position 1	Bicycle	28	0°
3.26	10 mm/h - Day	Position 1	Bicycle	28	45°
3.27	10 mm/h - Day	Position 1	Bicycle	28	90°
3.28	10 mm/h - Day	Position 1	Bicycle	56	0°
3.29	10 mm/h - Day	Position 1	Bicycle	56	45°
3.30	10 mm/h - Day	Position 1	Bicycle	56	90°
3.31	10 mm/h - Day	Position 1	Bicycle	84	0°
3.32	10 mm/h - Day	Position 1	Bicycle	84	45°
3.33	10 mm/h - Day	Position 1	Bicycle	84	90°
3.34	10 mm/h - Day	Position 1	Bicycle	112	0°
3.35	10 mm/h - Day	Position 1	Bicycle	112	45°
3.36	10 mm/h - Day	Position 1	Bicycle	112	90°
3.37	10 mm/h - Day	Position 1	Corner reflector	112	0°
3.38	10 mm/h - Day	Position 1	Corner reflector	56	0°
3.39	10 mm/h - Day	Position 1	Corner reflector	84	0°
3.40	10 mm/h - Day	Position 1	Corner reflector	112	0°

Test	Description	Sprinkler position	Target	Distance (m)	Angle
3.41	10 mm/h - Day	Position 1	LiDAR targets	28	0°
3.42	10 mm/h - Day	Position 1	LiDAR targets	56	0°
3.43	10 mm/h - Day	Position 1	LiDAR targets	84	0°
3.44	10 mm/h - Day	Position 1	LiDAR targets	112	0°
3.45	10 mm/h - Day	Position 1	Camera targets	28	0°
3.46	10 mm/h - Day	Position 1	Camera targets	56	0°
3.47	10 mm/h - Day	Position 1	Camera targets	84	0°
3.48	10 mm/h - Day	Position 1	Camera targets	112	0°
4.1	10 mm/h - Night	Position 1	Pedestrian	28	0°
4.2	10 mm/h - Night	Position 1	Pedestrian	56	0°
4.3	10 mm/h - Night	Position 1	Pedestrian	84	0°
4.4	10 mm/h - Night	Position 1	Pedestrian	112	0°
4.5	10 mm/h - Night	Position 1	Bicycle	28	0°
4.6	10 mm/h - Night	Position 1	Bicycle	56	0°
4.7	10 mm/h - Night	Position 1	Bicycle	84	0°
4.8	10 mm/h - Night	Position 1	Bicycle	112	0°
4.9	10 mm/h - Night	Position 1	Car	28	0°
4.10	10 mm/h - Night	Position 1	Car	56	0°
4.11	10 mm/h - Night	Position 1	Car	84	0°
4.12	10 mm/h - Night	Position 1	Car	112	0°
4.13	10 mm/h - Night	Position 1	Corner reflector	28	0°
4.14	10 mm/h - Night	Position 1	Corner reflector	56	0°
4.15	10 mm/h - Night	Position 1	Corner reflector	84	0°
4.16	10 mm/h - Night	Position 1	Corner reflector	112	0°
4.17	10 mm/h - Night	Position 1	LiDAR targets	28	0°
4.18	10 mm/h - Night	Position 1	LiDAR targets	56	0°
4.19	10 mm/h - Night	Position 1	LiDAR targets	84	0°
4.20	10 mm/h - Night	Position 1	LiDAR targets	112	0°
4.21	10 mm/h - Night	Position 1	Camera targets	28	0°
4.22	10 mm/h - Night	Position 1	Camera targets	56	0°
4.23	10 mm/h - Night	Position 1	Camera targets	84	0°
4.24	10 mm/h - Night	Position 1	Camera targets	112	0°
5.1	25 mm/h - Day	Position 2	Pedestrian	28	0°
5.2	25 mm/h - Day	Position 2	Pedestrian	28	45°
5.3	25 mm/h - Day	Position 2	Pedestrian	28	90°
5.4	25 mm/h - Day	Position 2	Pedestrian	56	0°
5.5	25 mm/h - Day	Position 2	Pedestrian	56	45°
5.6	25 mm/h - Day	Position 2	Pedestrian	56	90°

Test	Description	Sprinkler position	Target	Distance (m)	Angle
5.7	25 mm/h - Day	Position 2	Bicycle	28	0°
5.8	25 mm/h - Day	Position 2	Bicycle	28	45°
5.9	25 mm/h - Day	Position 2	Bicycle	28	90°
5.10	25 mm/h - Day	Position 2	Bicycle	56	0°
5.11	25 mm/h - Day	Position 2	Bicycle	56	45°
5.12	25 mm/h - Day	Position 2	Bicycle	56	90°
5.13	25 mm/h - Day	Position 2	Car	28	0°
5.14	25 mm/h - Day	Position 2	Car	28	45°
5.15	25 mm/h - Day	Position 2	Car	28	90°
5.16	25 mm/h - Day	Position 2	Car	56	0°
5.17	25 mm/h - Day	Position 2	Car	56	45°
5.18	25 mm/h - Day	Position 2	Car	56	90°
5.19	25 mm/h - Day	Position 2	Corner reflector	28	0°
5.20	25 mm/h - Day	Position 2	Corner reflector	56	0°
5.21	25 mm/h - Day	Position 2	LiDAR targets	28	0°
5.22	25 mm/h - Day	Position 2	LiDAR targets	56	0°
5.23	25 mm/h - Day	Position 2	Camera targets	28	0°
5.24	25 mm/h - Day	Position 2	Camera targets	56	0°
6.1	25 mm/h - Night	Position 2	Pedestrian	28	0°
6.2	25 mm/h - Night	Position 2	Pedestrian	56	0°
6.3	25 mm/h - Night	Position 2	Bicycle	28	0°
6.4	25 mm/h - Night	Position 2	Bicycle	56	0°
6.5	25 mm/h - Night	Position 2	Car	28	0°
6.6	25 mm/h - Night	Position 2	Car	56	0°
6.7	25 mm/h - Night	Position 2	Corner reflector	28	0°
6.8	25 mm/h - Night	Position 2	Corner reflector	56	0°
6.9	25 mm/h - Night	Position 2	LiDAR targets	28	0°
6.10	25 mm/h - Night	Position 2	LiDAR targets	56	0°
6.11	25 mm/h - Night	Position 2	Camera targets	28	0°
6.12	25 mm/h - Night	Position 2	Camera targets	56	0°
7.1	50 mm/h - Day	Position 3	Pedestrian	28	0°
7.2	50 mm/h - Day	Position 3	Pedestrian	28	45°
7.3	50 mm/h - Day	Position 3	Pedestrian	28	90°
7.4	50 mm/h - Day	Position 3	Bicycle	28	0°
7.5	50 mm/h - Day	Position 3	Bicycle	28	45°
7.6	50 mm/h - Day	Position 3	Bicycle	28	90°
7.7	50 mm/h - Day	Position 3	Car	28	0°
7.8	50 mm/h - Day	Position 3	Car	28	45°

Test	Description	Sprinkler position	Target	Distance (m)	Angle
7.9	50 mm/h - Day	Position 3	Car	28	90°
7.10	50 mm/h - Day	Position 3	Corner reflector	28	0°
7.11	50 mm/h - Day	Position 3	LiDAR targets	28	0°
7.12	50 mm/h - Day	Position 3	Camera targets	28	0°

Test	Description	Sprinkler position	Target	Distance (m)	Angle
4.1	10 mm/h - Night	Position 1	Pedestrian	28	0°
4.2	10 mm/h - Night	Position 1	Pedestrian	56	0°
4.3	10 mm/h - Night	Position 1	Pedestrian	84	0°
4.4	10 mm/h - Night	Position 1	Pedestrian	112	0°
4.5	10 mm/h - Night	Position 1	Bicycle	28	0°
4.6	10 mm/h - Night	Position 1	Bicycle	56	0°
4.7	10 mm/h - Night	Position 1	Bicycle	84	0°
4.8	10 mm/h - Night	Position 1	Bicycle	112	0°
4.9	10 mm/h - Night	Position 1	Car	28	0°
4.10	10 mm/h - Night	Position 1	Car	56	0°
4.11	10 mm/h - Night	Position 1	Car	84	0°
4.12	10 mm/h - Night	Position 1	Car	112	0°
4.13	10 mm/h - Night	Position 1	Corner reflector	28	0°
4.14	10 mm/h - Night	Position 1	Corner reflector	56	0°
4.15	10 mm/h - Night	Position 1	Corner reflector	84	0°
4.16	10 mm/h - Night	Position 1	Corner reflector	112	0°
4.17	10 mm/h - Night	Position 1	LiDAR targets	28	0°
4.18	10 mm/h - Night	Position 1	LiDAR targets	56	0°
4.19	10 mm/h - Night	Position 1	LiDAR targets	84	0°
4.20	10 mm/h - Night	Position 1	LiDAR targets	112	0°
4.21	10 mm/h - Night	Position 1	Camera targets	28	0°
4.22	10 mm/h - Night	Position 1	Camera targets	56	0°
4.23	10 mm/h - Night	Position 1	Camera targets	84	0°
4.24	10 mm/h - Night	Position 1	Camera targets	112	0°